DEVELOPMENT OF A LOW-COST, MULTIPLE-DIODE, CONTINUOUS LASER FOR PIV APPLICATIONS

by

Rajkumar Bhakta

Submitted in Partial Fulfillment
of the Requirements for the Degree of
Master of Science in Mechanical Engineering
with Specialization in Explosives Engineering

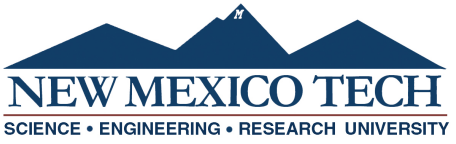

New Mexico Institute of Mining and Technology
Socorro, New Mexico
November, 2018

ABSTRACT

Particle image velocimetry (PIV) is an optical visualization and measurement technique that typically incorporates a single high-powered laser to illuminate seeded particles in a fluid flow. Standard PIV lasers are extremely costly and have limited pulse frequencies that reduce capabilities for high-speed, time-resolved imaging and measurement. The development of a multiple-diode laser system consisting of continuous lasers allows for flexible high-speed imaging with a wider range of test parameters. A series of experimental tests were conducted to compare the laser apparatus to a standard Nd:YAG double-pulsed PIV laser. Steady flow testing was performed in a free jet to compare the two systems and validate the accuracy of the multiple laser design. Unsteady flows generated by RP-2 detonators were examined to evaluate the limits of the design's capabilities for recording high-speed, time-resolved data. Steady flow PIV results indicate good similarity between the two laser systems. Unsteady flow testing revealed a camera limitation of 10 microsecond exposures. The key technical obstacle to this approach was laser design and calibration which will be discussed.

Keywords: PIV; continuous laser; high-speed flow; cost

ACKNOWLEDGMENTS

I would like to thank my academic and research advisor Dr. Michael Hargather. His teaching, support, and understanding during my undergraduate and graduate career has provided the necessary guidance I needed throughout my academic and personal life. You present an inspiration to always strive to be a better student and person. Thank you for providing constant opportunities where I can expand my knowledge and acquire new experience.

I would like to thank my friends and lab-mates for their support in my endeavors. Their individual knowledge and proficiencies was a large source of learning. Thank you for your many hours of help and support throughout my time at NMT. You made the difficult times in my life enjoyable.

Thank you to my parents, Bipin and Vaishali, and my sister, Heeta. You have provided every bit of support that I have needed. Thank you for enduring many hardships throughout your lives so that I can pursue higher education and ultimately live a better life. The magnitude of your sacrifice will never be forgotten.

Thank you to the Air Force and the Defense Threat Reduction Agency (DTRA) for sponsoring this research. Portions of this research were funded through Air Force STTR Phase I contract FA8651-17-P-0126 with Protection Engineering Consultants as the prime contractor with New Mexico Tech as a subcontractor. Portions of this research were funded through DTRA grant HDTRA1-14-1-0070.

CONTENTS

LIST OF TABLES

Table **Page**

LIST OF FIGURES

Figure **Page**

This thesis is accepted on behalf of the faculty of the Institute by the following committee:

Michael J. Hargather

Academic and Research Advisor

Peter Anselmo

Tie Wei

I release this document to the New Mexico Institute of Mining and Technology.

Rajkumar Bhakta September 4, 2018

CHAPTER 1

INTRODUCTION

1.1 Research Motivation

Various flow visualization methods provide distinct insights into fluid motion characteristics [1]. Turbulent motion in the wake of an explosive event is filled with interesting flow features that have yet to be fully defined [2]. Limited velocity measurements in a post-blast environment have been conducted with particle image velocimetry (PIV) and schlieren image velocimetry (SIV), and the greatest challenge is obtaining the time-resolved data necessary to understand this unsteady flow field. Various attempts have been made to develop time-resolved, low-cost PIV solutions for implementation in laboratory experiments [3]; however, these solutions typically incorporate a singular continuous laser for use in low speed flow events which is not powerful enough for high-speed events [4, 5, 6]. The primary goal of this research is to develop a low-cost PIV device for visualization and measurement of high-speed explosive flows generated by milligram-sized high explosive (HE) charges.

1.2 Literature Review

Various methods exist that enable the extraction of turbulent flow information in fluid flows. Pressure gauges are the traditional measurement approach in blast fields to provide information about transient explosive flow properties. These gauges, however, can interfere with the naturally evolving flow of the expanding blast because they must be physically located in the flow [7]. For the purpose of preserving the entirety of the flow, non-intrusive flow measurement methods are desired and ideal for the measurements here.

Three primary non-intrusive visualization techniques currently permit flow visualization and measurements: non-seeded optical, particle-seeded, and combination approaches [8]. Schlieren imaging, shadowgraphy, and their many variants, are the dominant types of non-seeded optical techniques. Particle-seeded methods include particle image velocimetry (PIV) and particle tracking velocimetry (PTV). Combination approaches involve seeding flows with energy, like electric discharge or heat, and visualizing that energy movement with optical techniques. Combination approaches will not be considered in this research since they perturb the flow by introducing energy thereby affecting fluid motion [8].

1.2.1 Particle Image Velocimetry

Particle image velocimetry (PIV) is an optical technique that allows for whole field, instantaneous velocity measurements of unsteady flows. PIV is a seeded visualization technique whereby small solid or liquid particles are embedded into a moving fluid and illuminated with a laser sheet [9]. By capturing the particle motion with a camera, cross-correlation image processing allows the extrapolation of fluid velocity from particle velocity provided a reasonable Stokes number [10]. The Stokes number measures how well suspended particles in a flow are coupled to fluid motion. The Stokes number is defined as:

$$Stk = \frac{t_0 u_0}{l_0}$$

where t_0 is the particle relaxation time, u_0 is the free stream fluid velocity, and l_0 is the characteristic length. A Stokes number below 1 indicates that the particles follow fluid motion well while a number greater than 1 indicates discrepancies between fluid and particle accelerations [11].

Using particles to observe fluid motion was a technique developed in the early 20th century by Ludwig Prandtl to visualize flow in a water tunnel [12]. Early digital PIV was limited to low-speed flows [13]. The advent of computer and camera technology allows PIV of faster moving flows. Hamel et al. showed good qualitative agreement between PIV measurements and CFD calculations on a supersonic open jet at Mach 2-3 [14]. Scarano conducted accurate PIV measurements in a wind tunnel at supersonic speeds ranging from Mach 1.8 to Mach 7 [15]. Some primary issues encountered with high-speed PIV include compressibility effects on seeding dispersal and uniform particle size distribution.

Imaging of explosive events is of interest in this research. Literature shows explosive features have been imaged with PIV [16, 17, 18]. Jenkins et al. showed PIV capability in explosive flows by performing analysis on aluminum particles accelerated by gram-sized RDX charges at a sampling rate of 15 Hz [16]. Jenkins et al. continued this work by performing particle velocity measurements on metallic particles accelerated by HMX charges [17]. Murphy et al. performed PIV measurements on exploding bridge wire (EBW) blast waves with a sampling frequency of 300 kHz but was only capable of capturing four image pairs (eight frames) [18]. These experiments were limited by the number of frames that could be captured or by low sampling frequencies.

These limitations are attributed to the typical pulsing feature of most PIV lasers which limit the amount of frames that can be captured during a high-speed event like an explosion[19]. Considering these disadvantages, an always-on or continuous laser would provide the widest range of test parameters allowing for a variety of low and high speed flow visualization. The lack of pulsing removes the need for synchronization between camera and laser, significantly reducing the complexity in equipment and operation. A continuous laser source allows for capturing more images but its low power output limits the flow velocities that can be captured since less light energy reflects off a particle per distance

traveled [20]. Due to the low power output of continuous lasers, larger exposure times are required to fully capture the flow particles. The longer light duration per exposure can produce particle streaking in images and thereby potentially induce error. This creates an upper velocity bound on the flows can be imaged [21]. Therefore, laser output power and exposure duration must be balanced to generate detailed, time-resolved PIV images.

Current PIV equipment is highly specialized, with a limited range of test parameters per type of laser [22]; however, advances in laser technology have lowered the overall cost of laser components. An inexpensive, innovative solution to observe fluid flow would make PIV a more useful and practical technique [23]. A continuous laser power source, like a laser diode, is therefore an ideal candidate for developing a low-cost PIV device for high-speed flow visualization.

1.2.2 Schlieren Image Velocimetry

Schlieren imaging is an optical technique that captures refractive index changes in transparent media by utilizing simple optics, a light source, and a knife edge [24]. Shadowgraphy operates in a similar manner but captures a shadow of the event without the use of a knife edge [25]. The data gathered from these techniques can be analyzed to obtain shock and gas propagation information from explosive events via streak imaging and edge detection [26, 27]. These techniques only provide partial flow velocity information. To obtain a more complete velocity field, schlieren image velocimetry can be conducted on the schlieren and shadowgraph images.

Schlieren imaging velocimetry (SIV) is a relatively new measurement technique and involves processing schlieren images with PIV algorithms. The algorithms track small eddies that act like PIV "particles" in the schlieren images. These eddies are generated by refractive index changes that result in localized light intensity variation that evolve throughout the observed transient flow. SIV is ideal for compressible or explosive flow fields because of the naturally occurring compressible-turbulence, which can be visualized with schlieren imaging. The technique was originally proposed and implemented manually by Townend before the development of computers, which now allow the process to be automated [28]. Jonassen et al. performed one of the first automated SIV measurements on a helium jet in air using commercially available PIV software [29]. Recent advances in SIV allows for schlieren images of explosive events to be processed using PIV algorithms providing velocity information in specific flow regions [30]. SIV algorithms are being developed to expand this research to allow full-field velocity measurements in high-speed environments [31].

1.3 Objectives of the Present Research

The primary objective of this research is to develop a continuous PIV laser system, at minimal cost, for high-speed, time-resolved flow applications. Goals include illuminating a 18 cm x 5 cm (7 in x 2 in) area with sufficient intensity for recording at one microsecond exposures. The developed PIV laser is compared to a commercial PIV laser system to quantify capability and identify limitations. Statistical analysis is conducted to quantitatively characterize the laser system. The ultimate goal is to allow imaging of high-speed explosive blasts to perform turbulent flow measurements within small-scale blasts inside a shock tube at New Mexico Tech [32].

CHAPTER 2

MULTI-DIODE LASER DEVELOPMENT

A Multi-diode Laser (MdL) consisting of 11 continuous, low-powered lasers was designed and constructed for this research. The device was developed to be used in conjunction with the Tunnel for High-speed Optical Research (THOR) to study unsteady, turbulent, explosively-driven flows [32]. The MdL was mounted vertically over THOR to generate a 2D light sheet for observing turbulent mixing in a post-detonation environment along the length of the tunnel. The singular 2D light sheet was formed by imbricating the individual lasers to mimic the same output as a traditional PIV laser. Although the strength of the laser demonstrated a limited range of applicability for accurate, time-resolved post-blast imaging, the diverse capabilities of the MdL allowed for successful high-speed flow visualization up to 10 microsecond exposures in limited regions of the post-blast environment and other high-speed flow fields.

2.1 Design

The Multi-diode Laser (MdL) was developed with a modular approach incorporating a laser-cut acrylic housing and 6 degree of freedom control over individual laser position and orientation. The MdL design integrated a repeating laser arrangement, allowing for easy future modifications and extensions. Using commercially available parts, eleven 200mW continuous lasers were placed in a staggered arrangement to generate an approximately 18-cm-long (7 inch) laser sheet in the region of interest in the THOR. The 11 laser sheets overlapped to emulate a singular laser sheet similar to the output of a commercial PIV laser. Figure 2.1 shows a 3D rendering of the MdL housing design alongside the final MdL assembly.

The structural components of the MdL were designed with laser-cut 6.35 mm (1/4 inch) acrylic and 2.54 cm x 2.54 cm (1 x 1 inch) 80/20 aluminum rail. The outer acrylic housing was 27.9 cm x 25.4 cm x 20.3 cm (11 inch x 10 inch x 8 inch) and incorporated mounting tabs for vertical and horizontal orientations. Slots were cut into the the side panels to fit and vertically adjust the lens housing. Individual lasers were fastened into six degree-of-freedom mounts that were connected to the 80/20 rail with sliding L brackets as shown in Figure 2.2. The design constraint for sequentially overlapping planes in a small region of interest required the lasers to be placed in a staggered formation as seen in Figure 2.3.

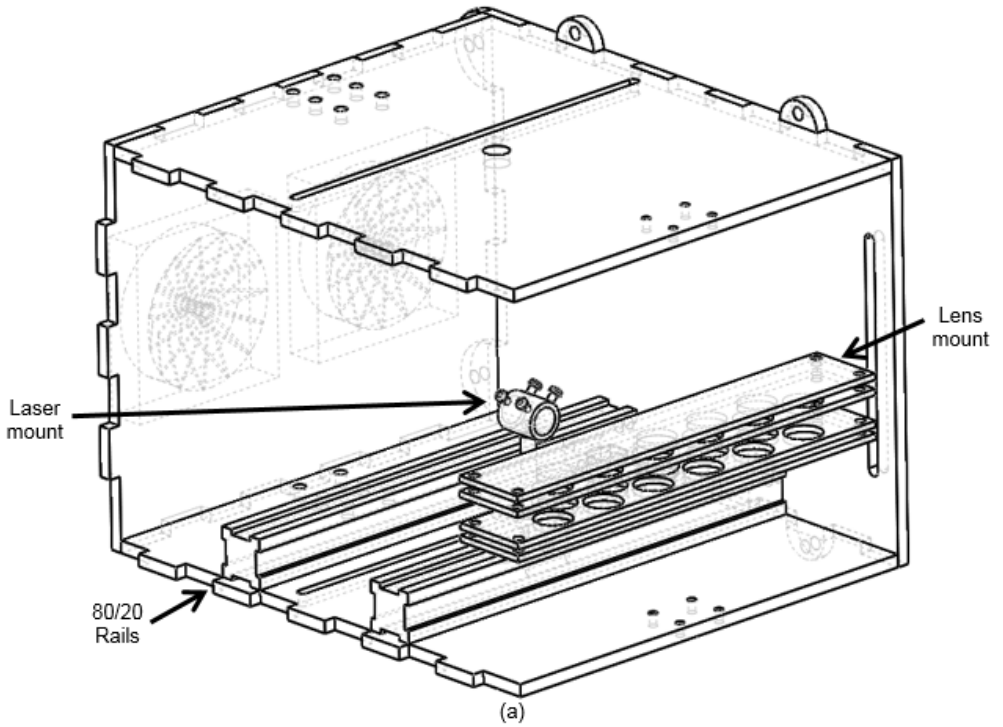

(a)

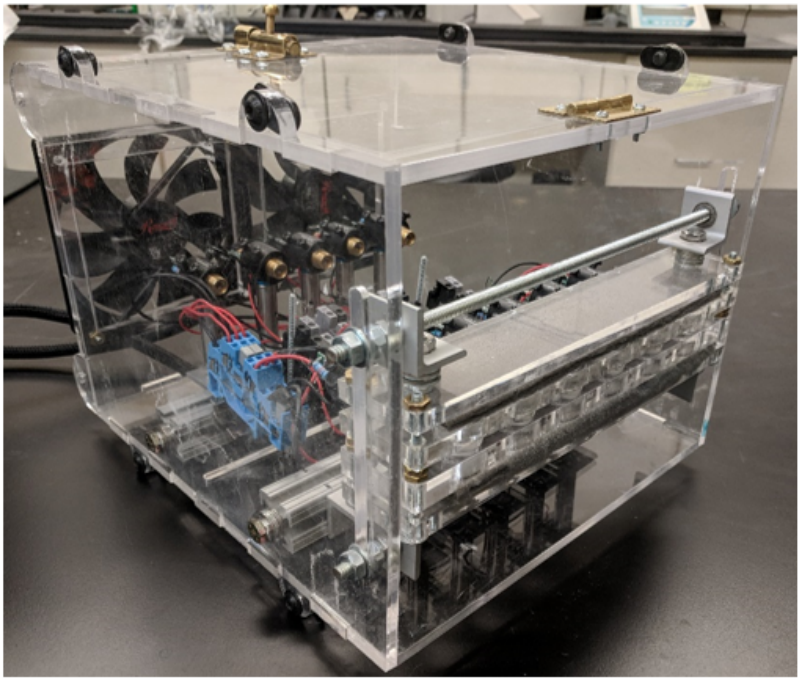

(b)

Figure 2.1: (a) Schematic of the Multi-diode Laser apparatus and (b) Completed MdL design.

The positive and negative cables for individual lasers were wired into

nearby terminals and then linked to a central terminal. The central terminal leads were connected to an external power supply via a small hole in the bottom panel. This allowed for easy replacement of defective or inoperable lasers. Two 120 mm fans were fixed to the back panel to cool the lasers and to exhaust any aerosolized particles from the housing. A hatchway was cut onto the top panel to provide access for readjustment and modification without requiring disassembly.

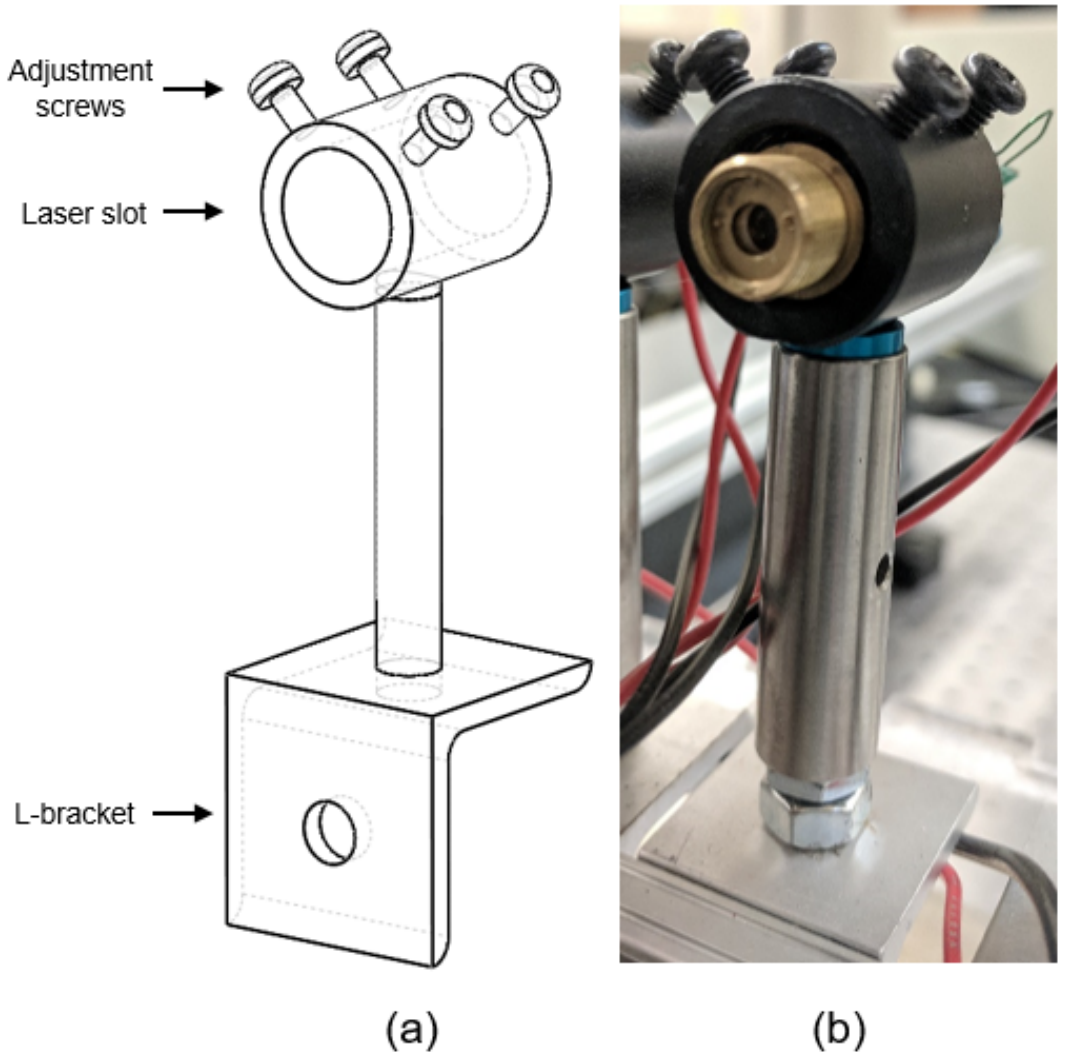

Figure 2.2: (a) Schematic of an individual laser mount fixed to an optical rod and secured onto an 80/20 rail via an L bracket. (b) Laser mount with diode installed.

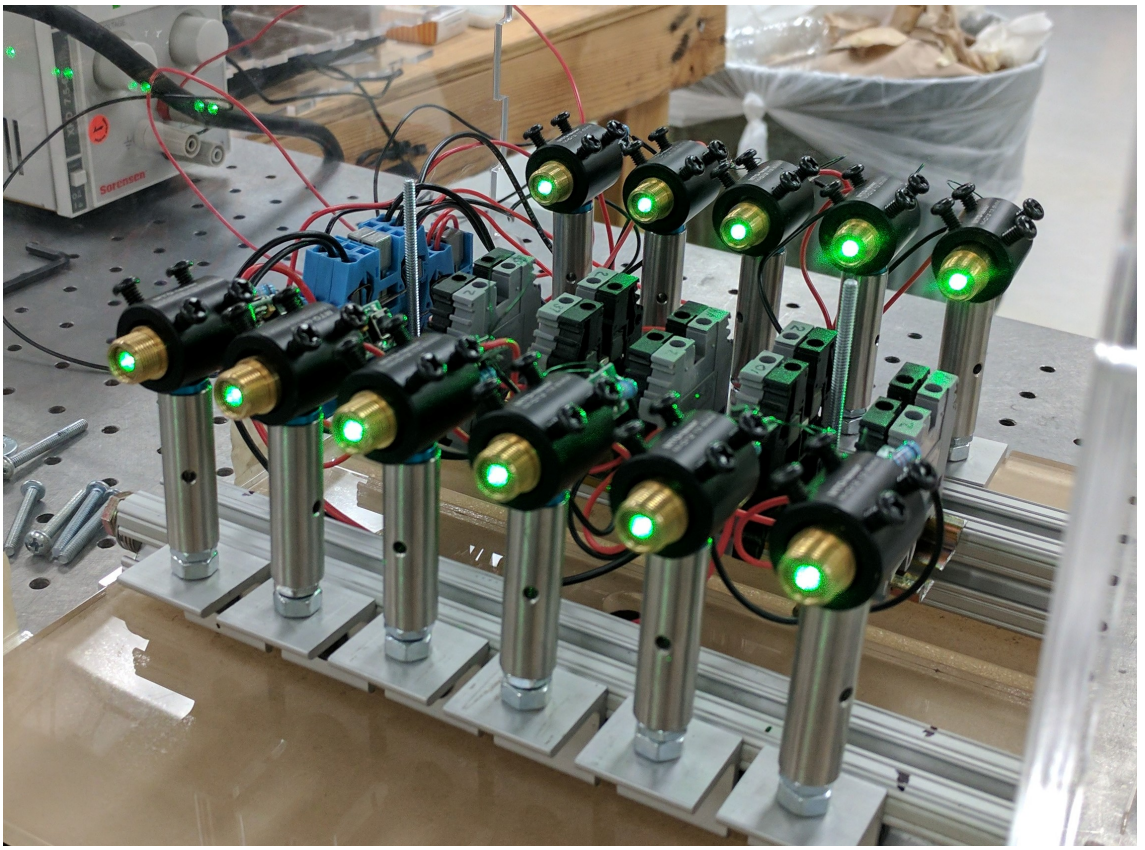

Figure 2.3: The staggered placement of laser positions to allow the formation of a singular light sheet.

2.1.1 Laser Specifications

A continuous laser was necessary and advantageous to support a range of test parameters allowing for flexible camera settings such as frame rate and exposure duration. To achieve low cost and low maintenance, laser diodes were chosen as the laser source. Desired operating requirements were to allow measurement of high-speed flows with a camera exposure of one microsecond or less to ensure particle position accuracy and minimize streaking. Three lasers of various power outputs, 50 mW, 100 mW, and 200 mW, were used to calculate the minimum light density needed to sufficiently illuminate seed particles in air and accurately track the particles using the commercial PIV software Insight4G from TSI [33].

To compare the varying power outputs of the lasers, a test series was conducted incorporating a single laser from each power category. Each laser beam passed through a 19 mm (3/4 inch) glass rod acting as a cylindrical lens, generating a 2D light plane. A concave lens collimated the light into a 2.54 cm (1 inch)

wide 2D light sheet for comparison. The operational voltage of the MdL was increased from 3.30 V to 3.50 V for greater illumination. The test setup is shown in Figure 2.4. Solid talc particles were aerosolized into the light sheet using a hand air pump that contained a fixed mass of particles per test. A high speed camera operating at 1 microsecond exposure was placed orthogonally to the light plane and captured images of the moving particles. A visual image histogram comparison between the various power categories indicated the 200 mw as the ideal candidate for satisfying the imaging criterion. Figure 2.5 shows visible talc particles at 1 microsecond exposure dispersed using the hand pump.

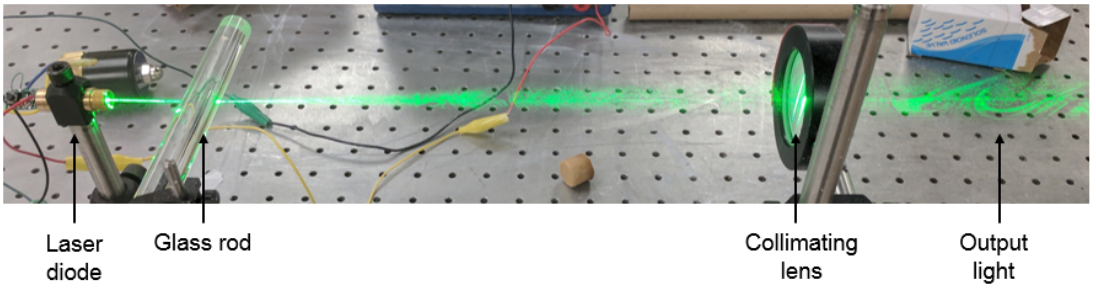

Figure 2.4: A single 200 mW laser traveling through a 19 mm (3/4 inch) cylindrical rod and collimated with a 2.54 cm (1 inch) concave lens.

Figure 2.5: Talc particles illuminated by a 200mW laser at 1 microsecond exposure. The image has been histogram stretched for visibility.

2.1.2 Cylindrical Lens Selection

A low-cost lens was required to transform the laser beam into a 2D laser sheet. Cylindrical lenses convert incoming light into an outgoing fan of 2D light.

Glass rods behave in a similar manner while costing significantly less. Glass rods of various sizes, 12.7 mm, 15.9 mm, and 19 mm (1/2 inch, 5/8 inch, and 3/4 inch), were used to quantify the light fan angle and determine appropriate lens size to satisfy design constraints. The width of the generated laser plane at different distances from the glass rods is shown in Figure 2.6. The fan angle decreases as the diameter of the glass rod increases. The 19 mm (3/4 inch) glass rod was chosen for the design to minimize loss of light on the edges of the MdL and reduce potential error in misaligned overlapping light sheets. The 19 mm lens also satisfies the physical constraint of generating a 18-cm-long laser sheet from approximately 25-50 cm above THOR.

To construct the lenses, a 25.4 cm long (1 ft), 19 mm (3/4 inch) diameter glass rod was cut into 11 approximately equal lengths with a diamond saw. The large lens sizes required the lenses to be arranged in a staggered formation to match its corresponding laser. An alignment plate was designed to hold individual lenses in position relative to their individual laser diode and prevent tilting. The lenses were wedged between two flat acrylic plates to brace the lenses in position. Due to slight variations in the lens lengths, the flat plates were lined with 6.35 mm (1/4 inch) foam to ensure sufficient compression was applied to all lenses. The lens housing was attached to the front of the main MdL housing with threaded rods fitted into slots and tightened into position. Figure 2.7 shows the lens housing schematic and final design.

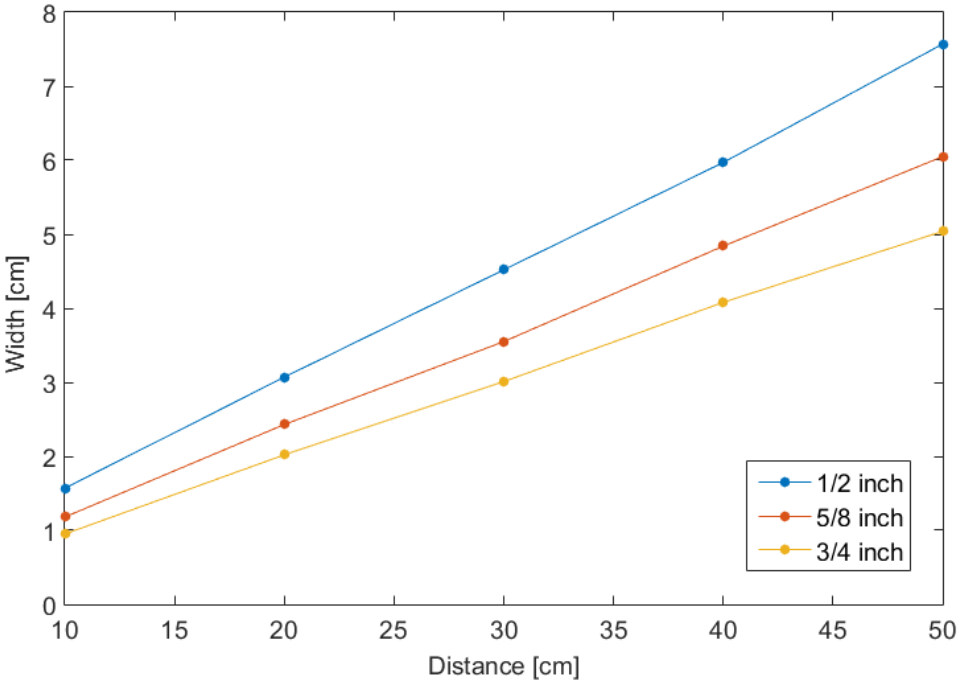

Figure 2.6: The width of laser sheets are various distances using different lenses.

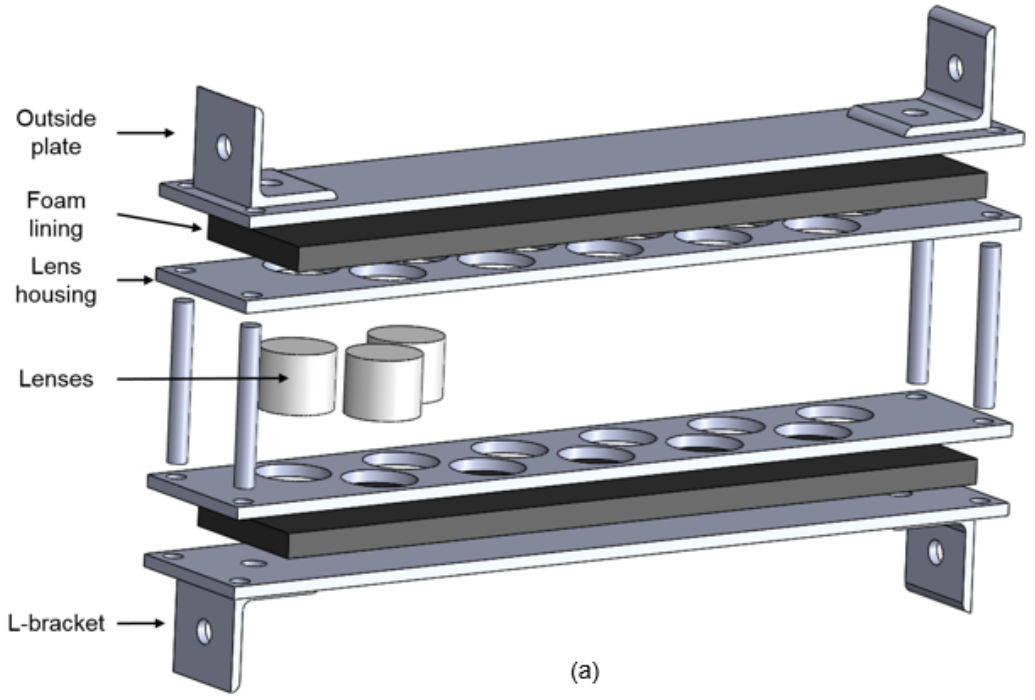

(a)

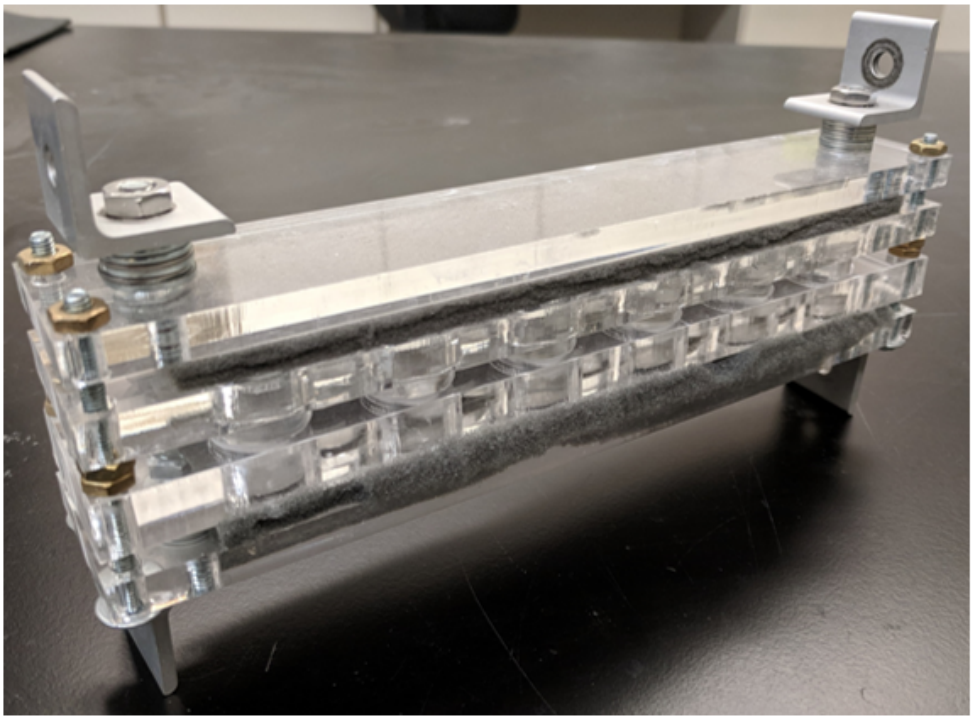

(b)

Figure 2.7: (a) Exploded view of lens housing schematic. (b) Fully assembled lens housing.

2.2 Alignment

Each laser required precise alignment to establish a combined laser sheet. As shown in Figure 2.2, individual lasers were adjusted into the correct position and orientation with 6 DOF mounts. The horizontal axis was controlled by sliding the laser mount along the rail. The vertical axis was controlled with a threaded rod to raise and lower the entire laser module. The distance from the cylindrical lens was controlled by sliding the laser into or out of the housing. The laser rotated to control roll. Four adjustment screws placed on the top of the individual laser mounts allowed for fine pitch and yaw adjustment. A small piece of foam was added to the bottom of all lasers before being inserted into their respective mounts. The foam elevated the laser allowing for greater control over pitch and yaw during adjustment.

To produce a singular laser sheet, individual laser sheets were arranged into position using two targeting boards. The target boards were etched with 11 targets at the required spacing to overlap all lasers. The distance between the boards spanned the width of the region of interest in THOR, about 5 cm (2 inches). By aligning each laser beam to intersect its respective targets on both boards, all laser beams could be fixed to the same two-dimensional plane. Figure 2.8 shows this alignment procedure and Figure 2.9 shows the outcome of the alignment. The entire lens housing can be translated vertically to ensure all lasers contact their respective lenses. Individual cylindrical lenses can be slightly adjusted to ensure proper positioning between respective lasers and lenses.

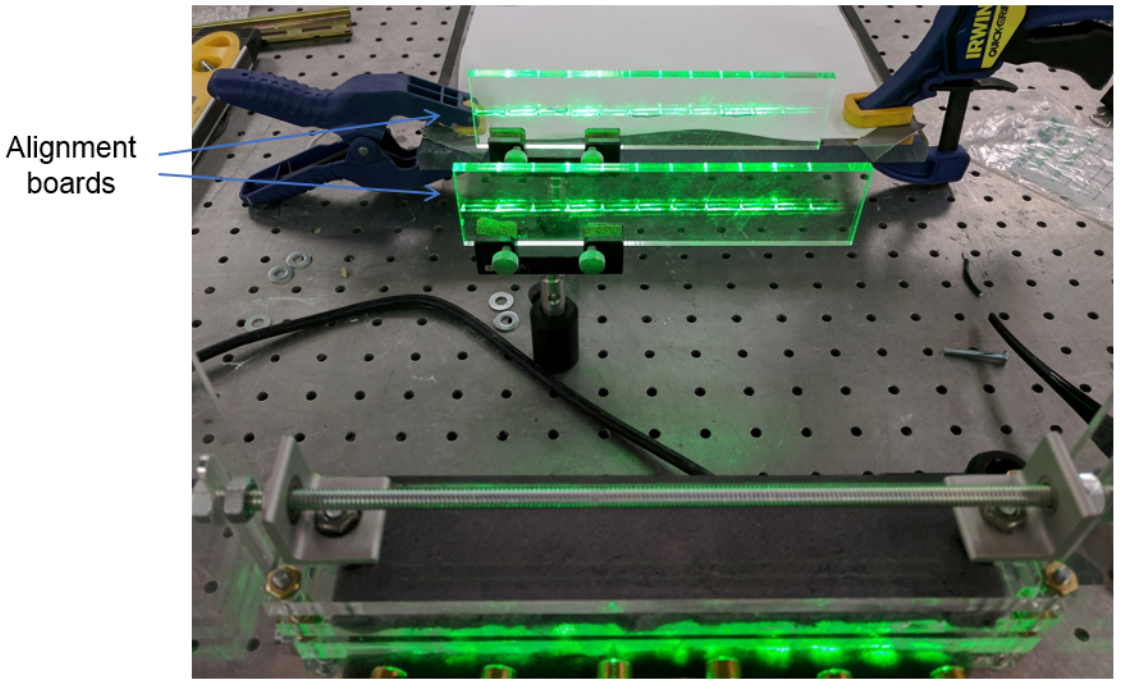

Figure 2.8: Two acrylic boards with laser etched targets were used to align lasers.

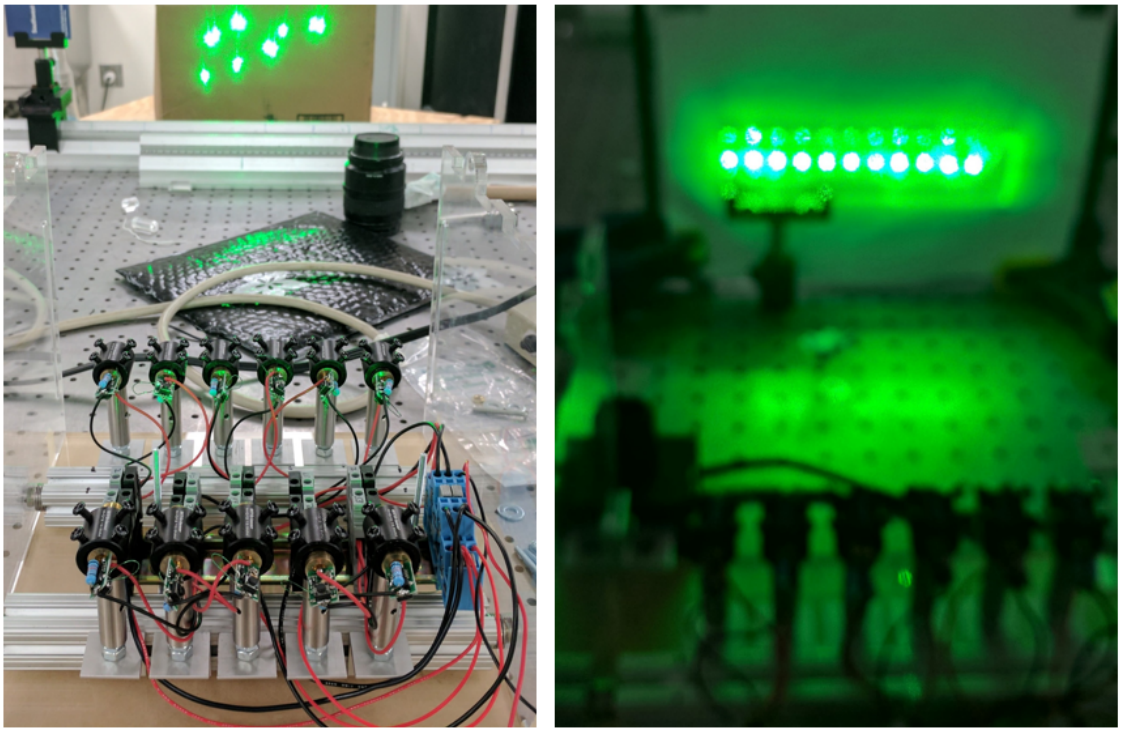

(a) (b)

Figure 2.9: Laser beam positions (a) before and (b) after alignment.

CHAPTER 3

EVALUATION OF MULTI-DIODE LASER

3.1 Comparison with Nd:YAG Laser

A series of experiments were conducted to determine initial Multi-diode Laser (MdL) capabilities. Liquid particles were aerosolized in a steady flow illuminated by the MdL and recorded using a Photron SA-X2 high-speed camera. The experiments were replicated using a commercially available New Wave Solo 200XT-15 Hz Nd:YAG (Neodymium-doped yttrium aluminum garnet) laser and TSI camera for comparison. All tests were analyzed using the commercial software Insight4G by TSI. The primary objective of this test series was to compare the performance of the MdL to the Nd:YAG Laser in a steady, repeatable environment. The Nd:YAG laser properties are described in Table 3.1. Secondary objectives included identification of an optimal particle for low-exposure conditions and suitable dispersal techniques.

Table 3.1: Properties and specifications of New Wave Solo 200XT-15Hz Nd:YAG laser

Repetition rate (straddle)	3 - 15 Hz
Pulse width	< 3-5 ns
Energy stability	$\pm$ 4%
Pulse energy for each pulse	30 mJ
Beam divergence	< 3 mrad
Beam pointing	< 100 μrad
Jitter	$\pm$ 0.5 ns
Beam Diameter	2.5 mm

3.2 Steady Flow Comparison with Water Particles

3.2.1 Setup

Two experimental setups were constructed for measuring steady flow seeded with water particles. The first setup is shown in Figure 3.1 consisting of the MdL, liquid atomizer, and Photron SA-X2 high-speed camera. All components were placed on an optical table for easy orthogonal alignment. The atomizer dispersed water particles vertically through a 2.54 cm (1 inch) nozzle. The MdL was situated on a platform placed horizontally in relation to the atomizer. The Photron SA-X2 high-speed camera was mounted perpendicular to the flow plane. A 22.7 liter (6 gallon) air compressor provided the necessary air pressure for the atomizer.

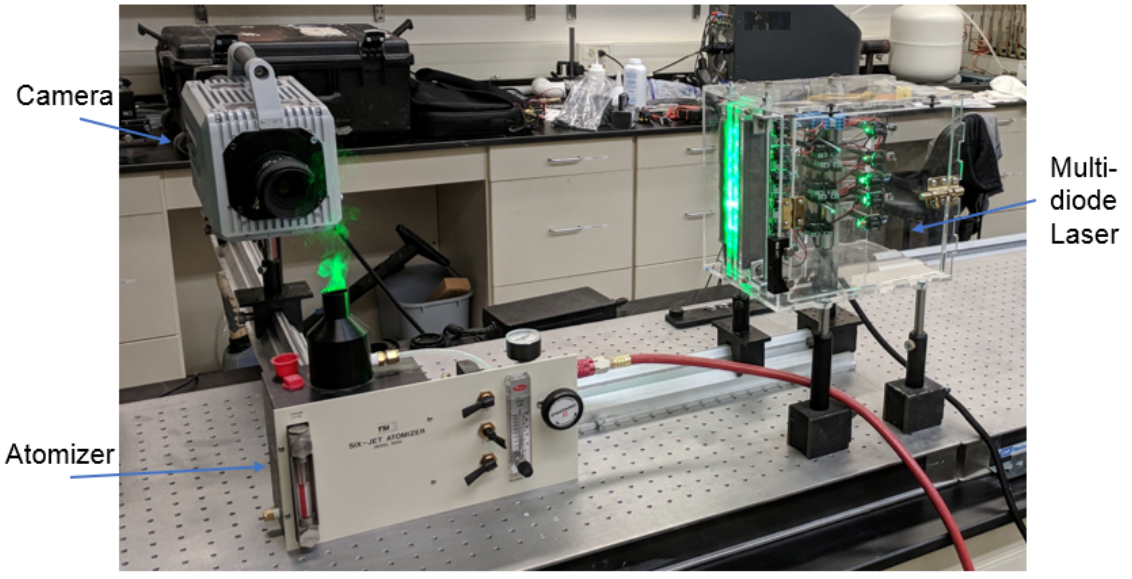

Figure 3.1: The MdL test setup with high-speed camera and atomizer

The second setup consisting of the Nd:YAG laser, liquid atomizer, and Insight4G camera is shown in Figure 3.2. The MdL and the high-speed camera from the first setup were replaced by the Nd:YAG laser and a TSI camera, respectively. The distances from the atomizer to the Nd:YAG laser and TSI camera were adjusted to achieve the same spatial resolution as in the first setup; the TSI camera has a larger pixel sensor than the SA-X2, so it is positioned farther from the flow in this setup.

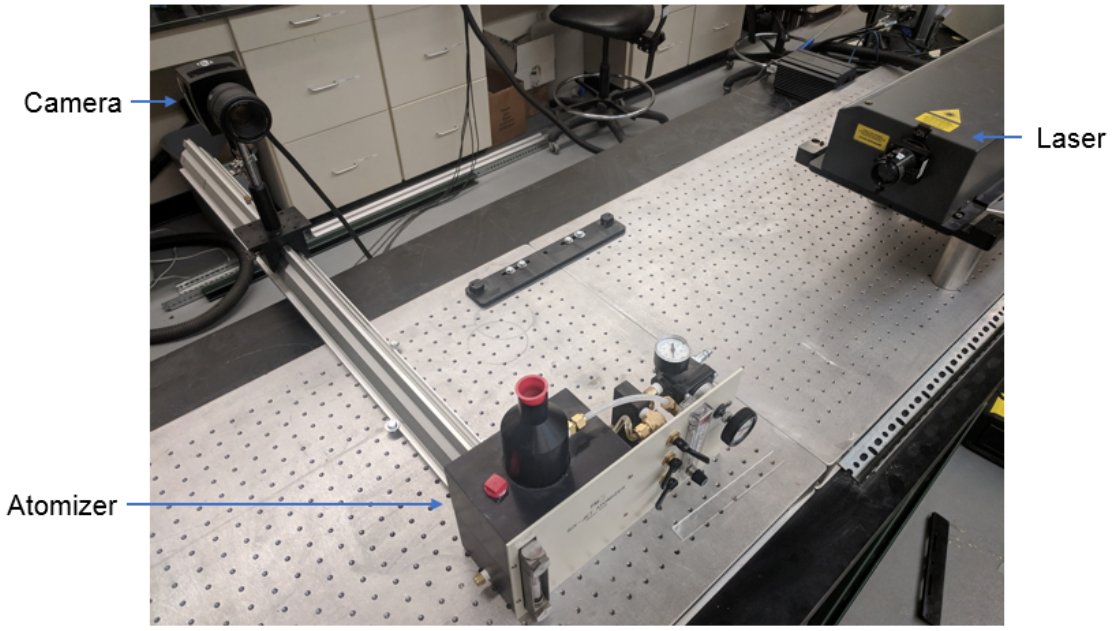

Figure 3.2: The Nd:YAG laser test setup with TSI camera and atomizer

A 6-jet TSI atomizer (model 9306) with a nozzle diameter of D = 25.4 mm (1 inch) was used to disperse water particles in a steady, repeatable flow. Only two jets were initiated to generate particles for tracking and to avoid superabundance of water droplets. The 275 kPa (40 psi) air pressure supplied by the compressor was throttled to 69 kPa (10 psi) at the atomizer inlet valve. The particle dilution was set to 20 L/min to balance particle velocity with adequate seeding density. Table 3.2 shows the atomizer operating parameters.

Table 3.2: Operating parameters of TSI atomizer

Pressure	20 psi
Particle dilution	20 l/min
Number of engaged jets	2
Water temperature	25 °C

The camera distances relative to the atomizer were determined by matching spatial resolution between both cameras to reduce discrepancies in post-processing. The TSI camera records at a resolution of 2048 x 2048 pixels while the SA-X2 records at 1024 x 1024 resolution. The edge of the atomizer nozzle was used to align the two image sizes onto the same 1024 x 1024 region of interest. The Photron SA-X2 operated at 10,000 fps and 100 us exposure capturing sequential

images. The TSI camera operated at approximately 15 Hz capturing pairs of images 100 us apart. The exposure of the TSI images is controlled by the laser pulse duration to be 5 ns. A timing diagram for the TSI camera is shown in Figure 3.3.

Data collected using the SA-X2 camera spans a total collection time of one second due to the high sampling rate of 10,000 fps. Image pairs were extracted from the data set by skipping 20 frames between image pairs, creating a larger time step between image pairs. This provides a more random data set and allows for a better time-resolved average. The Nd:YAG system records pairs of images at approximately 15 Hz, averaging data over 33 seconds.

The MdL system captures images in a sequential, continuous form while the Nd:YAG system captures images with a larger time step between itâĂŹs image pairs. The resulting images captured by the Nd:YAG laser are more random due to the large time steps between the image pairs. This provides a true average data set for the Nd:YAG system compared to the MdL system. The small time step between the MdL system image pairs captures ongoing eddy structures as they propagate through the flow. This can result in asymmetry in the averaged flow data since multiple instances of the same eddy structures are being captured due to the high frame rate of the camera. However, the higher sampling rate of the MdL system demonstrates the ability to collect better time-resolved measurements required in high-speed unsteady flows.

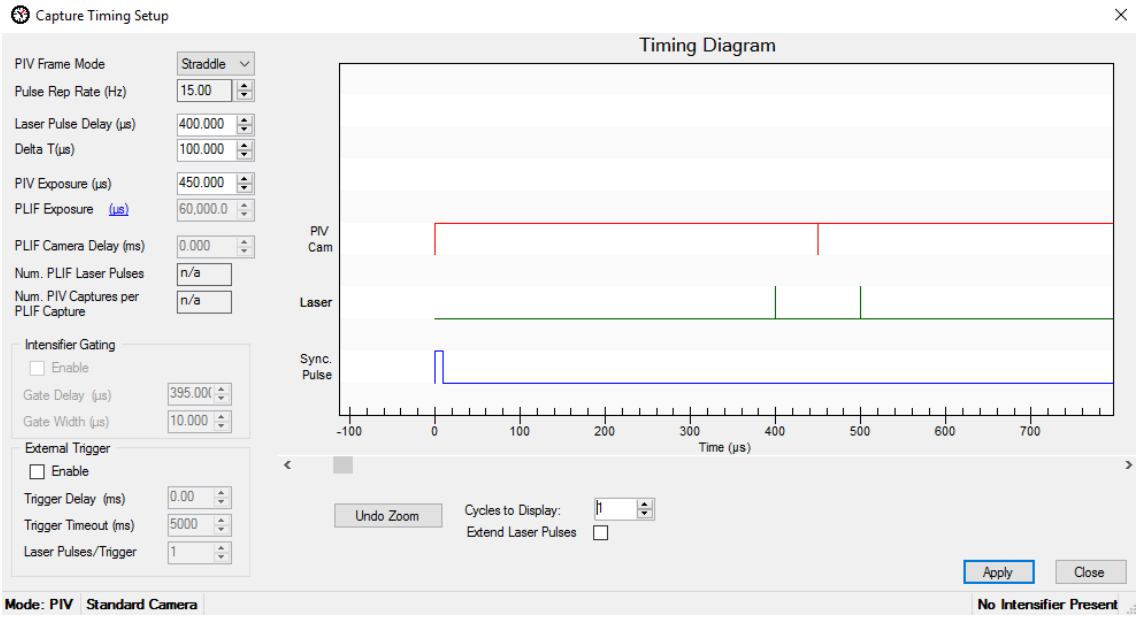

Figure 3.3: The timing diagram for the Nd:YAG laser.

3.2.2 Water Droplet Flow

A series of tests were conducted whereby 500 image pairs per test (1000 total images) were recorded. Each test was replicated using the two laser systems. To compare the two systems, the image pairs were processed using Insight 4G software by TSI to compute an average velocity magnitude field. A contour map of the average velocity magnitudes from each system is shown in Figures 3.4 and 3.5.

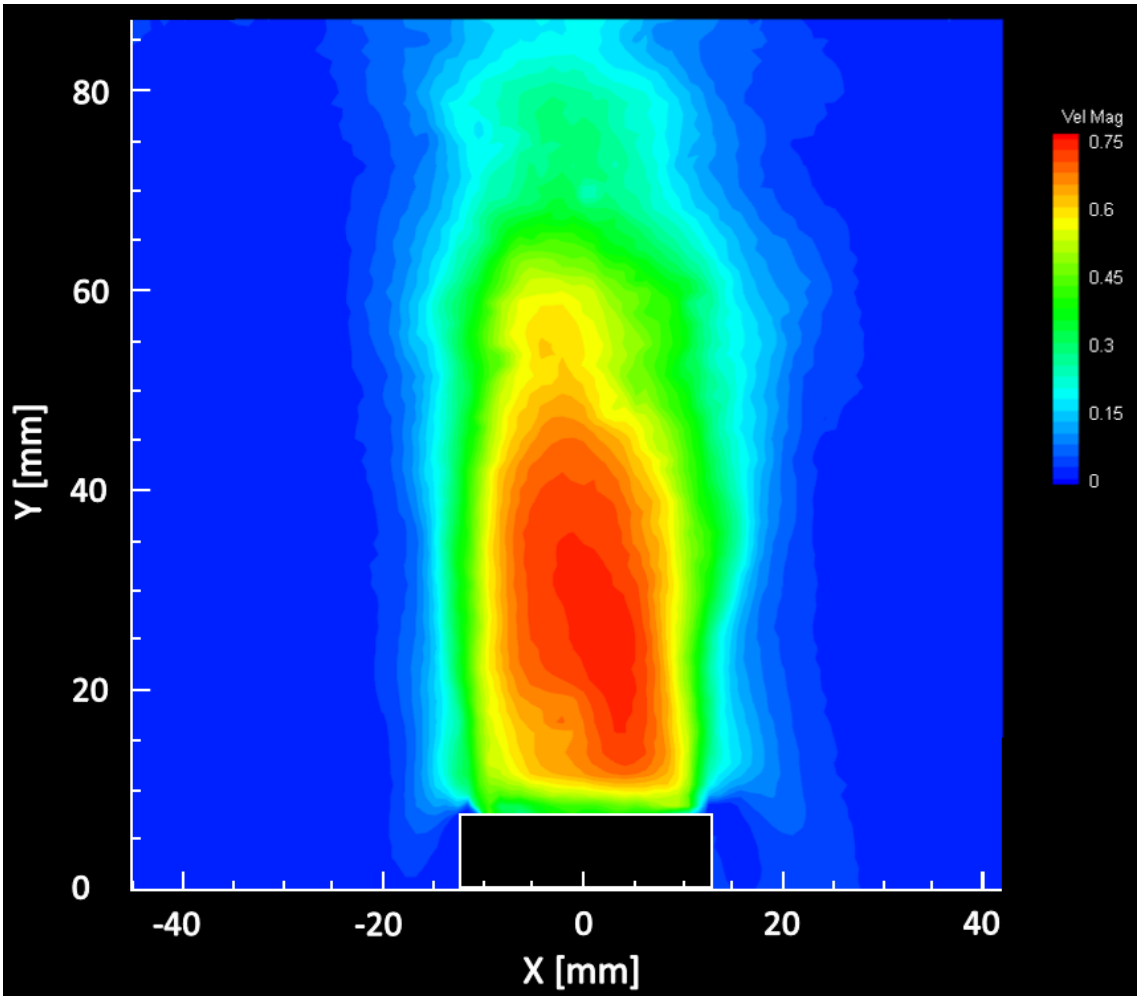

Figure 3.4: The averaged velocity field calculated from 500 image pairs measured using the MdL.

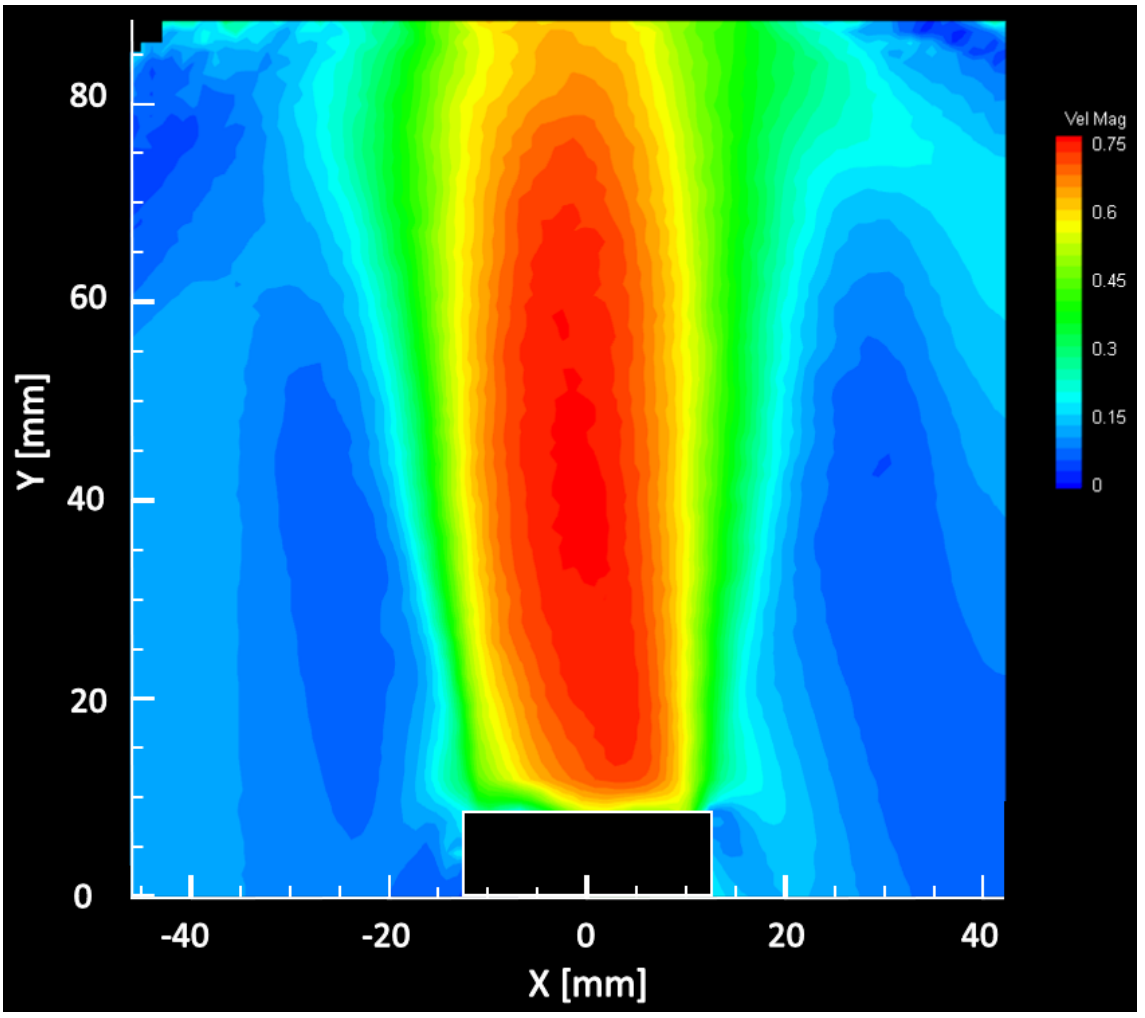

Figure 3.5: The averaged velocity field calculated from 500 image pairs measured using the Nd:YAG laser.

All images were processed using Insight 4G software by TSI. A comparison was conducted between interrogation window sizes to determine the smallest ideal interrogation window. Figure 3.6 shows a velocity profile at location x/D of 0.5 using varying window sizes. A 24 x 24 pixel interrogation window was the smallest window size that provided similar velocity measurements to larger window sizes. Therefore, a 24 x 24 pixel interrogation window was used for all water droplet analysis.

The images were processed using a fast fourier transform (FFT) correlation technique. Post-processing was conducted to remove all velocity vectors outside three standard deviations. Recursive filling was applied with a 5 x 5 window size to fill in missing velocity vectors. The camera and lens differences between the SA-X2 and TSI camera allowed for a limited range of focus and was the primary constraint for choosing a spatial resolution of 11.4 pix/mm.

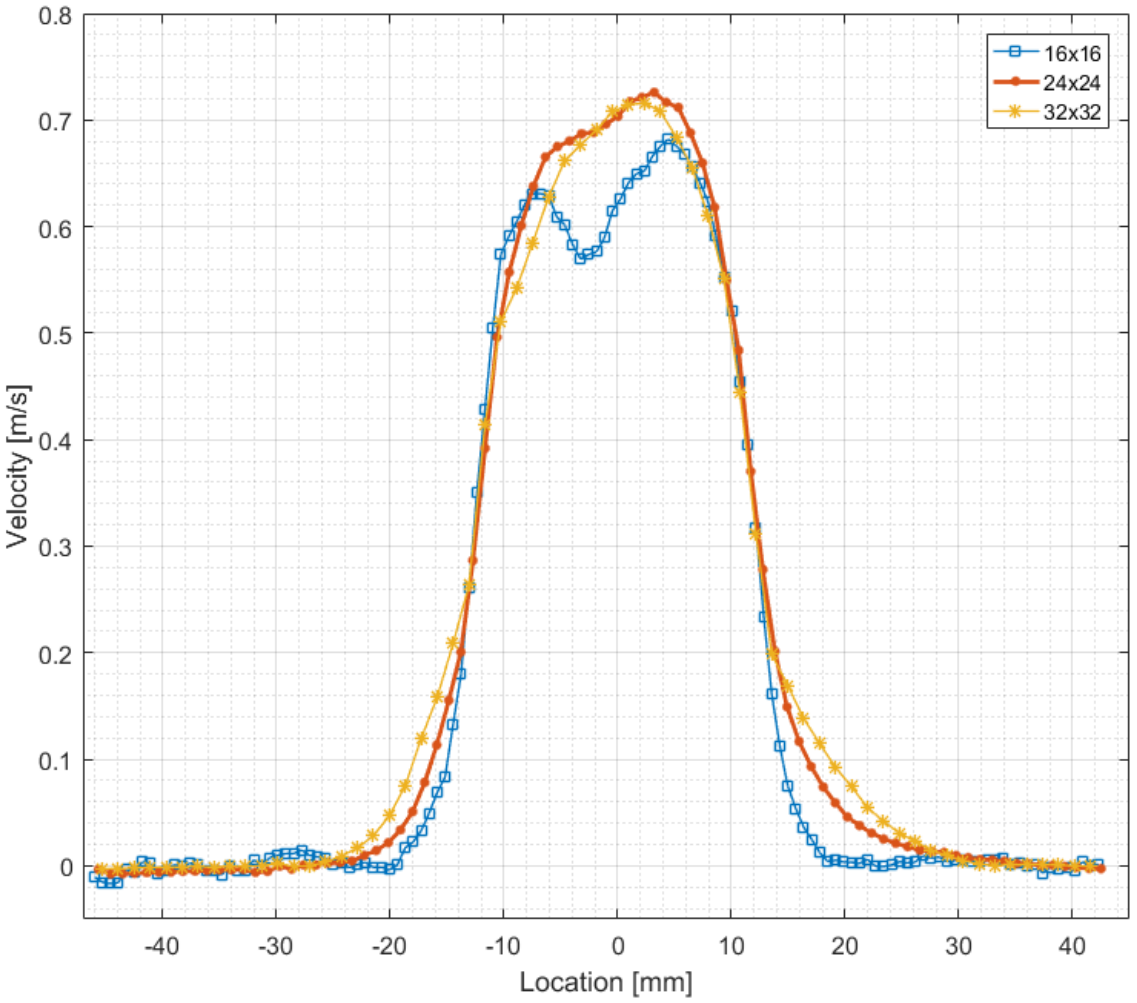

Figure 3.6: A comparison between different interrogation window sizes for optimal PIV analysis.

3.2.3 Statistical Analysis

The objective of this section is to use statistical tools to compare the data sets obtained from two laser systems and quantify the differences in their measurements. Statistical techniques used to compare the data set include mean, variance, standard deviation, and Welch's T-test.

Horizontal rows from the mean velocity magnitude shown in Figures 3.4 and 3.5 were extracted at varying locations along the length of the flow. Velocity profiles were created from these rows using the mean vertical velocity component. Four velocity profiles were compared between the two systems and shown in Figure 3.7. The profiles show good agreement in locations where x/D is less than one. At distances greater than x/D = 1, the MdL shows lower velocity magnitudes but maintains curve similarity with the Nd:YAG profile.

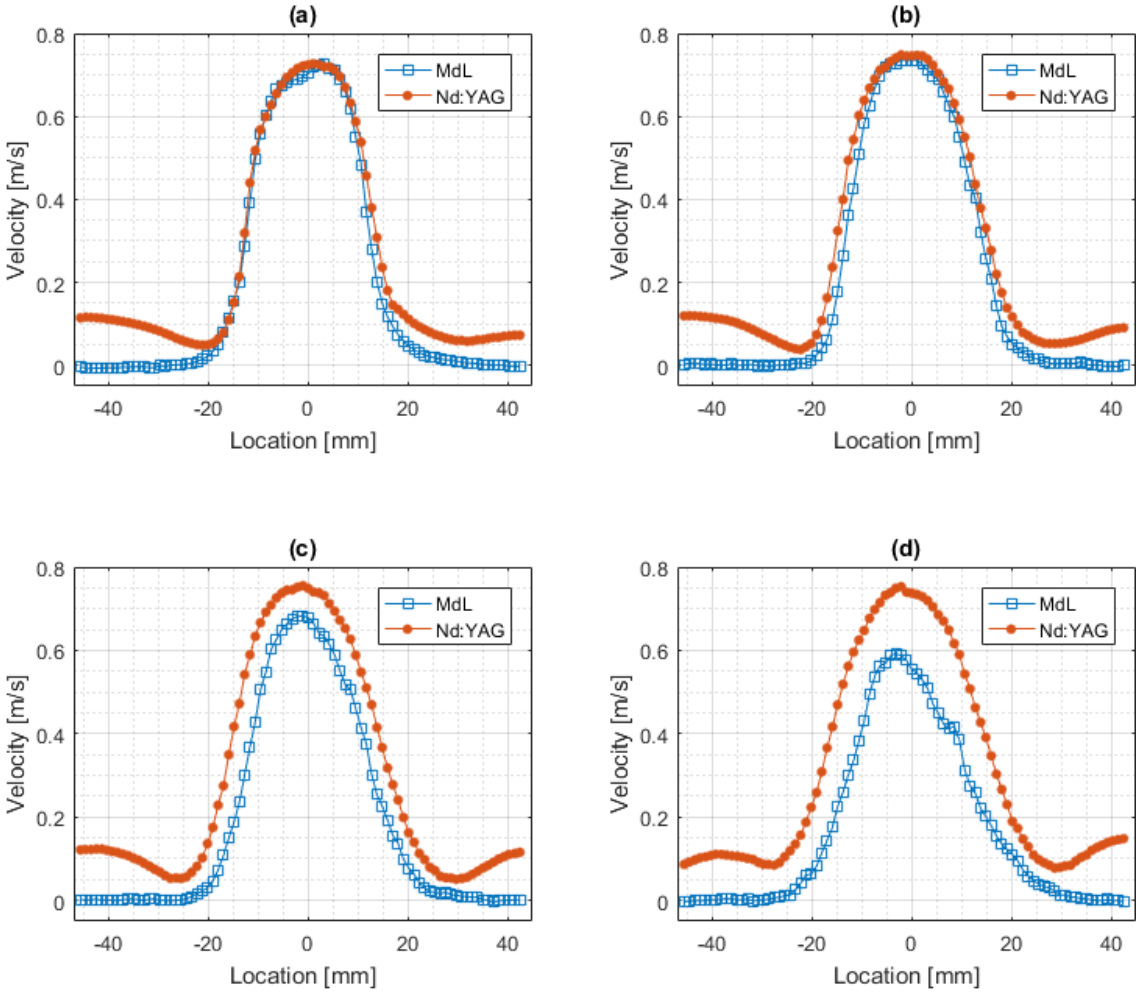

Figure 3.7: Velocity profiles of both laser systems at various x/D distances from the nozzle exit. (a) x/D = 0.5 (b) x/D = 1 (c) x/D = 1.5 (d) x/D = 2.

Before performing statistical calculations, irrelevant data values were removed from both data sets. During PIV analysis, the region of interest included portions of the unseeded background resulting in ambient noise vectors. Image processing techniques were implemented to identify a boundary between the jet flow and the background. 500 images were combined to create a single image to visualize light intensity in the data set. A 5 percent threshold was applied to differentiate the background noise from the bright pixels in the fluid flow. The threshold identifies a linear jet boundary at the exit of the nozzle. This initial linear boundary can be expanded to define the edge of the jet in the entire image. The resulting binary image is shown in Figure 3.8. Red lines in the image indicate the edge of the jet flow boundary. The boundary reveals a jet opening angle of approximately 12 degrees, as expected in a low velocity jet with low Reynolds number [34]. Velocity vectors outside this boundary were not considered in the statistical analysis comparison.

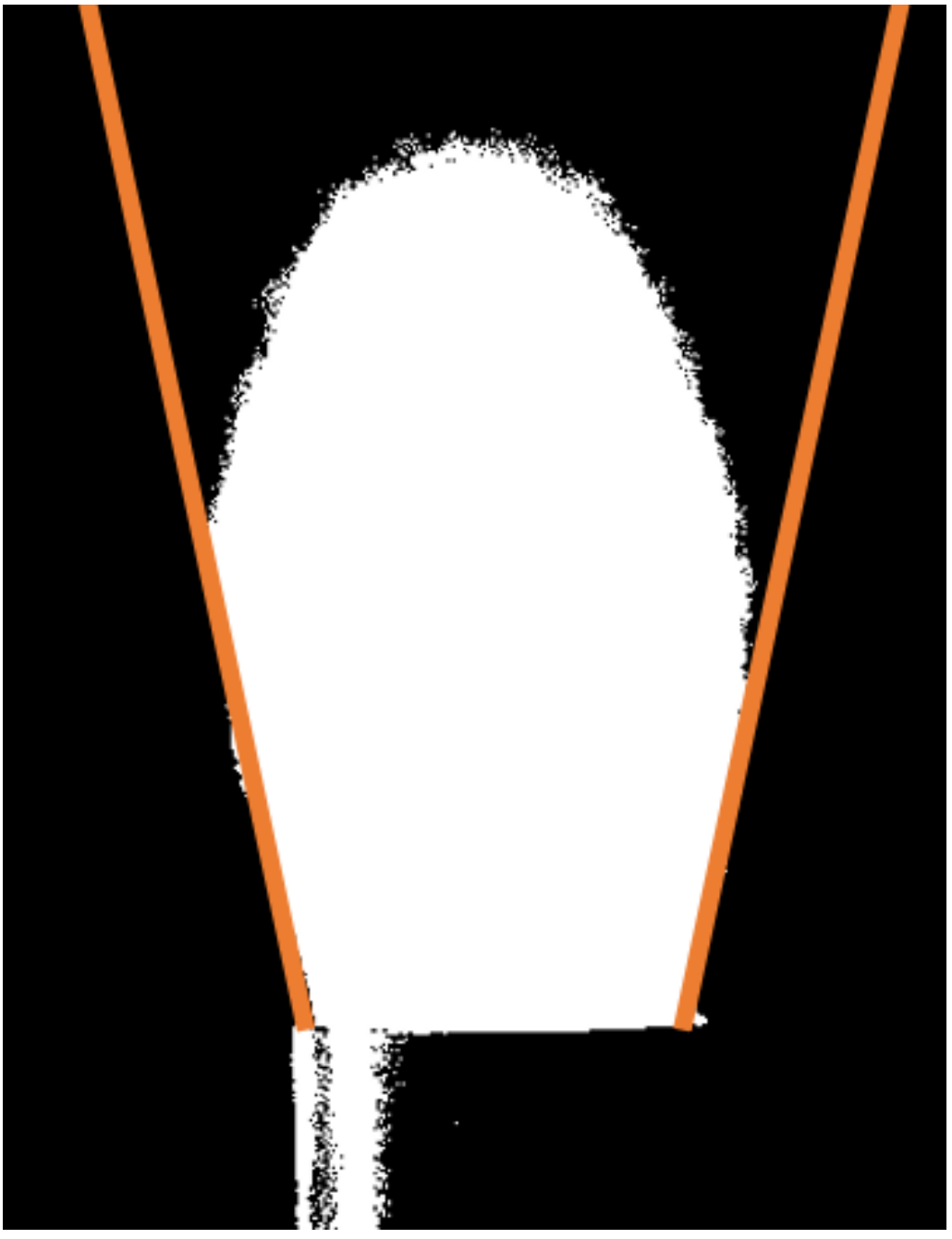

Figure 3.8: Binary image of the jet nozzle with a 5 percent threshold. Red lines denote the edge of the flow boundary.

A Reynolds number of 1,265 was computed at location x/D = 1 using the maximum centerline velocity of 0.75 m/s at standard temperature and pressure. The low Reynolds number indicates a laminar to early transitional fluid flow. Large eddy propagation speeds were calculated at the x/D distances shown in Figure 3.7 using a maximum centerline velocity of 0.75 m/s. The equation used

to calculate the propagation speed is:

$$Eddy\,speed = \frac{Jetwidth}{0.75} \tag{3.1}$$

Equation 3.1 outputs a time step that is synonymous with Nyquist frequency, identifying the minimum time step necessary to successfully capture turbulent velocity fluctuations in the largest eddies at maximum velocity [35]. The camera operating parameters of 10,000 Hz result in a time step of one millisecond between frames, fully satisfying the required time steps shown in Table 3.3.

Table 3.3: Large eddy propagation speeds at various x/D distances calculated with a maximum velocity of 0.75 m/s

x/D	Jet width (mm)	Large eddy propagation speeds (ms)
0.5	32	42.7
1	37	49.3
1.5	41	54.7
2	45	60.0

A T-test analysis was performed to compare the means of the two data sets. The hypothesis being tested by the T-test is:

$$H_o : \mu_1 = \mu_2$$

$$H_a : \mu_1 \neq \mu_2$$

Welch's T-test is a variation of the standard T-test that does not assume the data sets have equal variances. It is more reliable and robust when considering data sets that have differing variances and sample sizes. Welch's T-test and the associated degrees of freedom can be computed using:

$$t = \frac{\overline{X}_1 - \overline{X}_2}{\sqrt{\frac{s_1^2}{N_1} + \frac{s_2^2}{N_2}}} \tag{3.2}$$

$$v \approx \frac{(\frac{s_1^2}{N_1} + \frac{s_2^2}{N_2})^2}{\frac{s_1^4}{N_1^2 v_1} + \frac{s_2^4}{N_2^2 v_2}} \tag{3.3}$$

A two-tailed T-test analysis was conducted since the velocity mean must be within a range of values. An alpha value of 0.05 was used. The results from the T-test analysis are shown in Table 3.4. A T value that falls between $\pm$T critical value indicates that the null hypothesis (equal means) cannot be rejected. A T value outside the critical value range shows that the means of the data sets are not

similar. The velocity profiles at locations x/D = 0.5,1 have equal means within the set statistical parameters whereas the profiles located at x/D = 1.5,2 do not have equal means. This conclusion can be observed in Figure 3.9 which illustrates the centerline velocity decay from both systems.

Table 3.4: Results from Welch's T-test analysis

	Velocity profile 1		Velocity profile 2		Velocity profile 3		Velocity profile 4	
	MdL	Nd:YAG	MdL	Nd:YAG	MdL	Nd:YAG	MdL	Nd:YAG
Mean (m/s)	0.4999	0.5279	0.4810	0.5349	0.3843	0.5124	0.3184	0.5019
Variance (m/s)	0.0525	0.0435	0.0593	0.0452	0.0537	0.0483	0.0350	0.0444
Observations	32	32	36	36	41	41	44	44
v	61		69		80		85	
T value	0.5109		1.0001		2.5682		4.3189	
T critical (two-tail)	1.9996		1.9949		1.9901		1.9883	

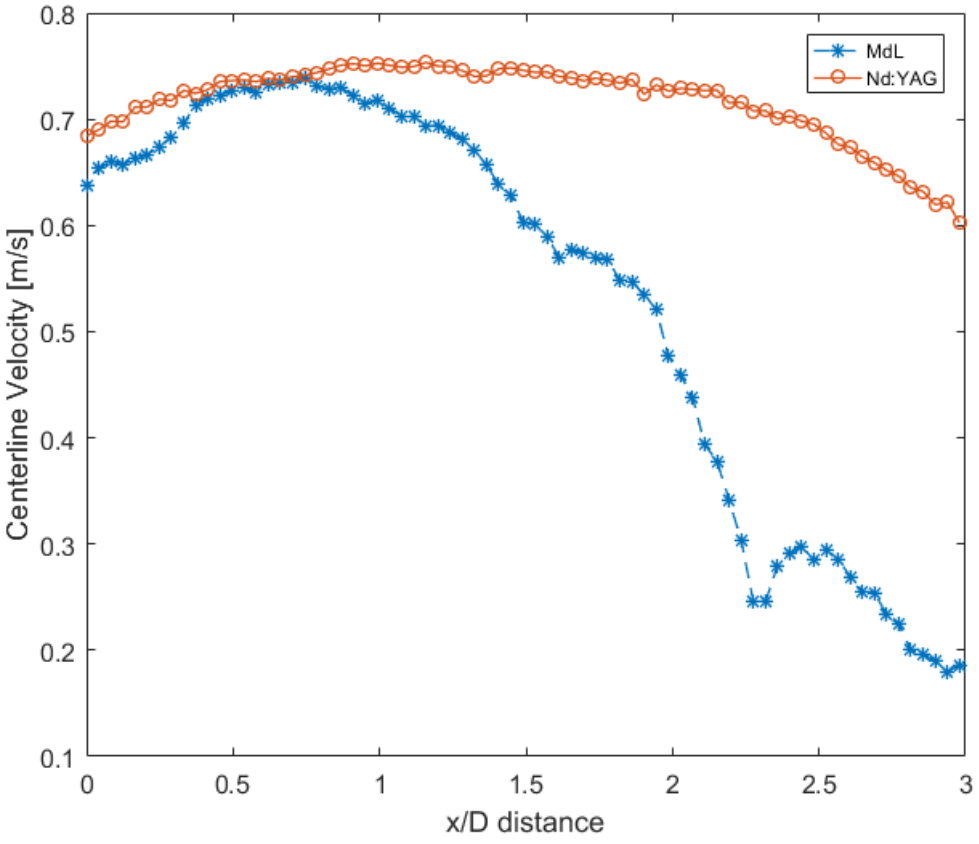

Figure 3.9: MdL and Nd:YAG centerline velocities at various x/D distances.

The decreasing agreement between the two curves at further distances can be attributed to a variety of factors including: MdL laser alignment, varying laser

quality, and decreasing particle density. Misalignment in adjacent lasers could result in illumination of particles not along the center cross section of the flow. By illuminating particles not along the center cross section, slower moving particles are illuminated and therefore provide inaccurate velocity data in those regions. This most likely explains the discrepancies between the two systems observed at x/D distances greater than 1 where the MdL centerline velocity decreases rapidly compared to the Nd:YAG centerline velocity. Additionally, decreasing particle density at further distances from the exit of the nozzle make particle tracking with a lower power laser more difficult. Less illuminated particles result in a lower number of observations per interrogation window and therefore increase measurement error. A low-quality laser with ineffective optics or lower operating voltage would result in similar error since less particles are illuminated with the lower light output. Although the centerline velocity magnitude decreases with increasing x/D, the variance between the calculated values remains relatively constant as shown in Table 3.4. Statistical analysis of the data sets obtained by both laser systems indicates good similarity between the data sets provided sufficient illumination and particle density.

3.2.4 Error Analysis

Many sources can contribute to potential error in PIV calculations but, total error can be broadly defined as a combination of systematic and random errors. Turbulent fluctuation velocity was computed instead of random error for this research. The systematic error, or bias error, is defined here as error offset from true value and can be calculated by:

$$\frac{x_{observed} - x_{true}}{x_{true}} \tag{3.4}$$

Turbulent fluctuation velocity was calculated using:

$$F = \sqrt{\sum_{i}^{n} \frac{(x_{observed} - x_{observed,mean})^2}{N}} \tag{3.5}$$

The systematic error calculation is performed between the averaged measurements of both systems to compare precision between the two data sets. The fluctuation error in velocity measurements is calculated to quantify fluctuations in the consecutive velocity measurements.

The bias error calculated using Equation 3.4 is shown in Figure 3.10. The complete averaged velocity profile for both lasers was used in determining bias error. Bias error is high in regions outside the flow field due to ambient noise. The error indicates a trend of increasing bias error with increasing x/D.

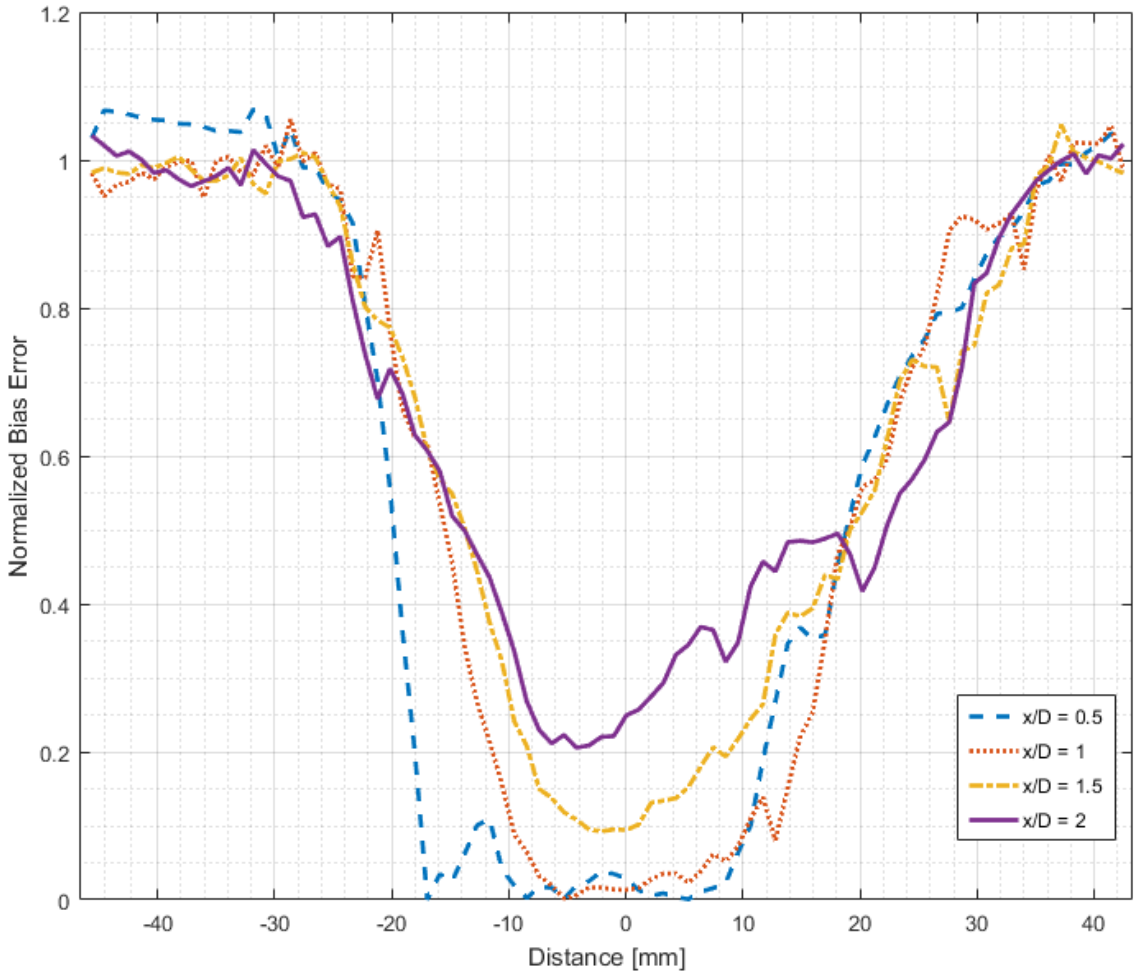

Figure 3.10: Normalized systematic error for various velocity profiles.

Fluctuation error calculated using Equation 3.5 is shown in Figures 3.11 and 3.12. Individual velocity vectors were classified as the observed data set. The mean velocity magnitude of the individual vectors was used as the observed mean value. Near the center regions where the flow resides, the fluctuation error between the MdL and the Nd:YAG laser are comparable. Additionally, the error curves from both lasers demonstrate similar shape and magnitude at varying distances.

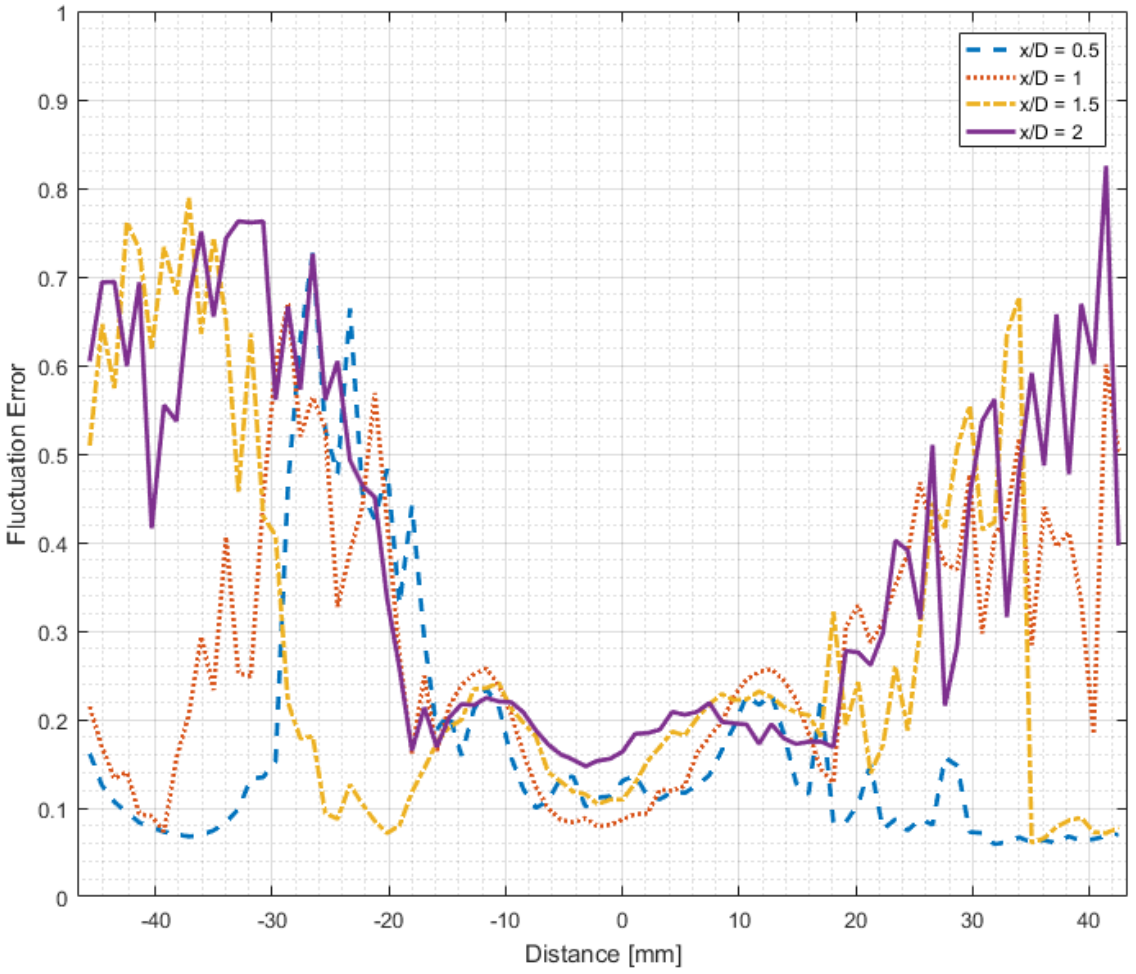

Figure 3.11: Velocity fluctuation error in MdL measurements across multiple velocity profiles.

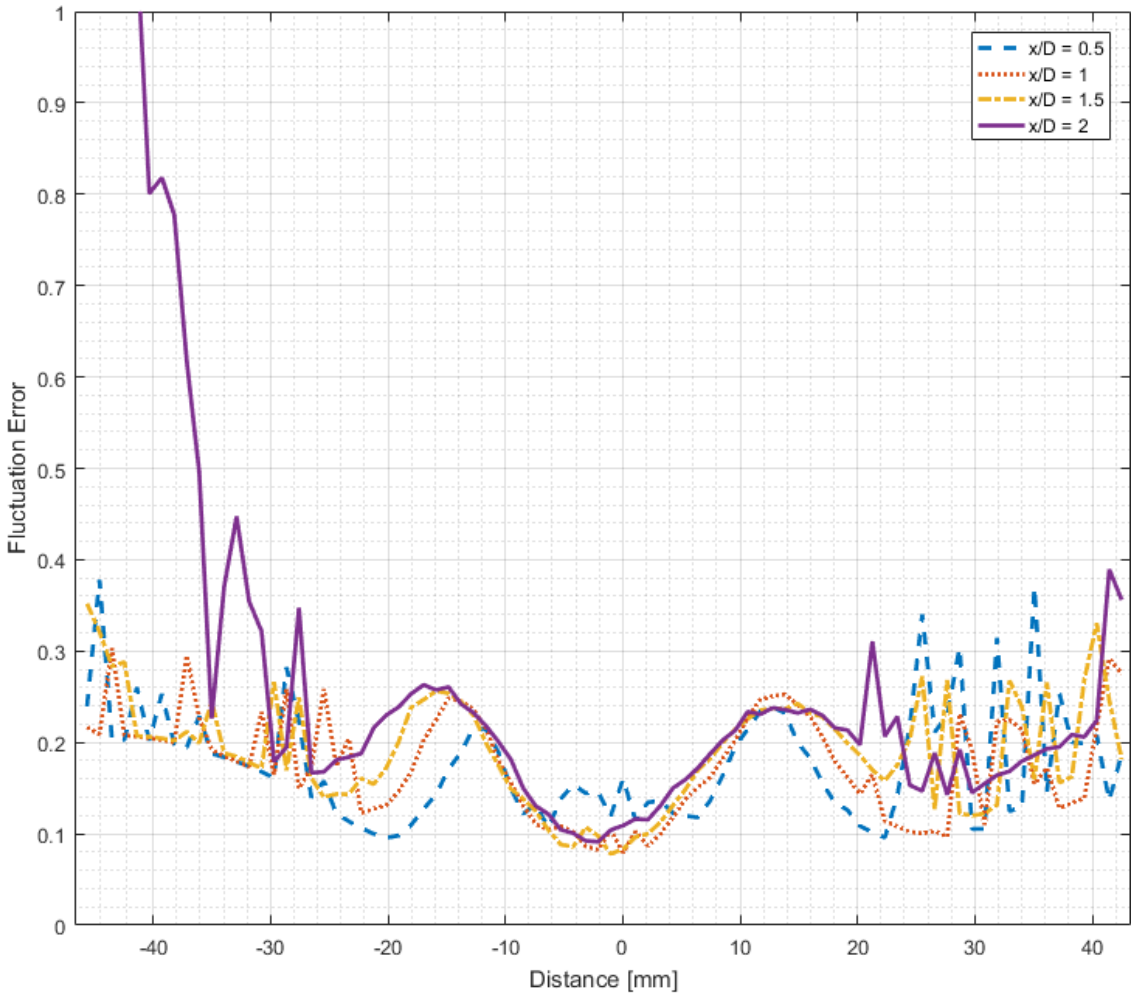

Figure 3.12: Velocity fluctuation error in Nd:YAG laser measurements across multiple velocity profiles.

CHAPTER 4

UNSTEADY FLOW IN SHOCK TUBE

The Tunnel for High-speed Optical Research (THOR), a 100 mm x 100 mm square shock tube, was used to observe post-blast turbulent mixing generated with milligram-sized high explosive (HE) charges. An image of THOR is shown in Figure 4.1. THOR's test section included clear viewing windows 17.8 cm long (7 inches) and 5.1 cm wide (2 inches) on all four sides of the tube for observing the blast event. The MdL was mounted vertically above the shock tube and the camera was placed orthogonal to the light sheet. Figure 4.2 shows the MdL and camera placements around THOR. Solid particles distributed with a custom-made diffuser were used. Images were processed with Insight 4G software by TSI.

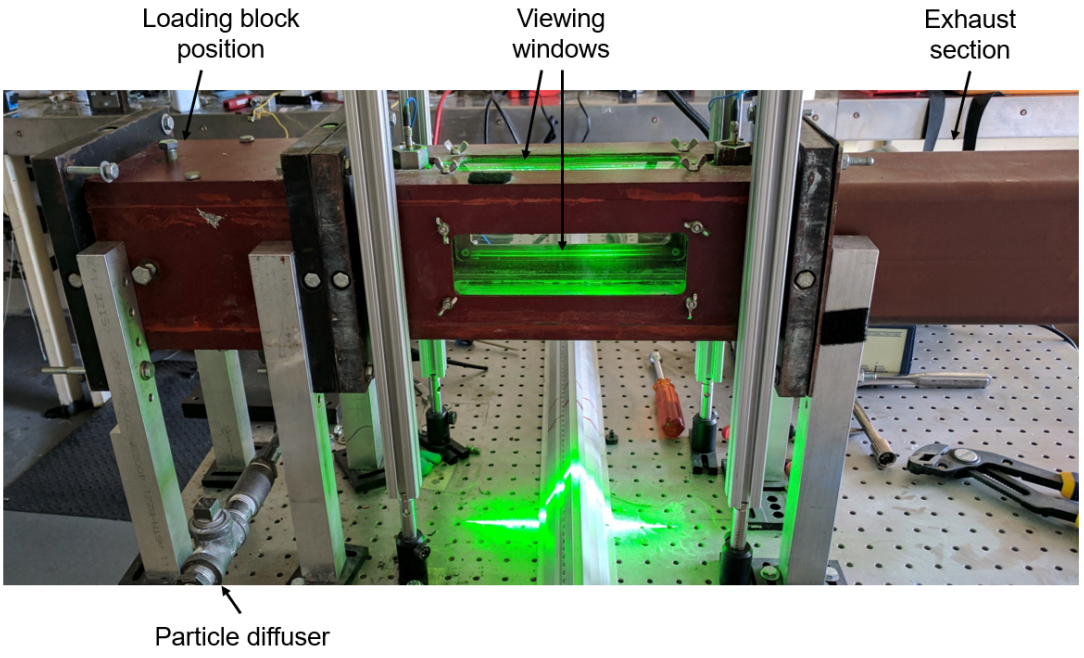

Figure 4.1: General design features of THOR and particle diffuser placement.

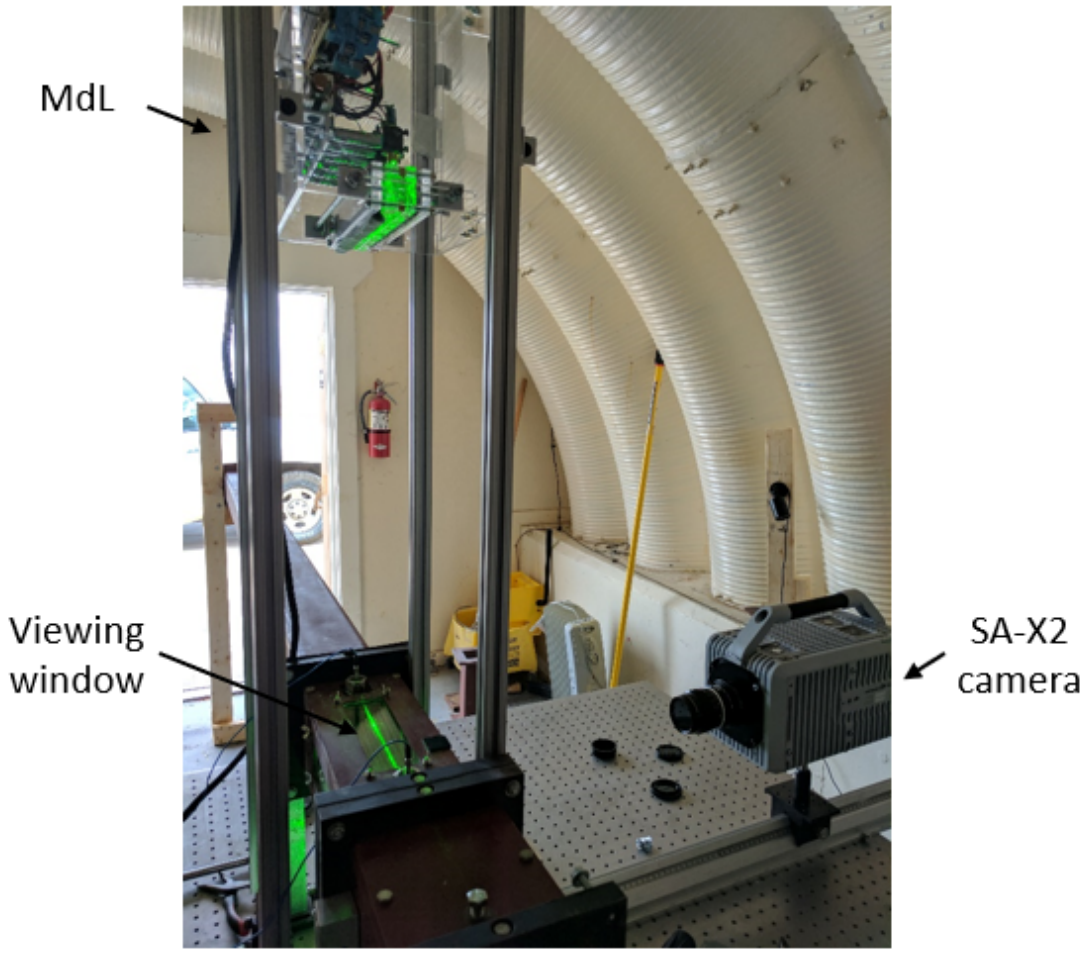

Figure 4.2: Explosive testing setup showing placement of MdL and Photron SA-X2 camera.

4.1 Particle Dispersal

A custom-made solid particle diffuser was developed to seed the airflow inside the THOR. Figure 4.3 shows the diffuser design. The particle diffuser contained three primary sections: the valve control, the seeding chamber, and the ball bearing chamber. Two 6.3 mm (1/4 inch) valves, one electric solenoid valve and one ball valve, were used to throttle the airflow at the entrance. The electronic valve was joined directly to a 22.7 liter (6 gallon) air compressor. The 40 psi regulated air from the compressor was further suppressed at the ball valve, allowing for a slower airflow at the diffuser exit. The electronic valve allows for remote control of particle dispersal. The seeding chamber consists of a 6.3 mm (1/4 inch) NPT Tee pipe fitting. Solid particles were loaded into the chamber through the removable top joint as shown in Figure 4.3. The ball bearing chamber contained

4.5 mm ball bearings which disrupt incoming clusters of solid particles and generate a more fine, uniform seeding at the nozzle exit. Thin metal meshes were placed at the exit region openings to keep the ball bearings in the apparatus.

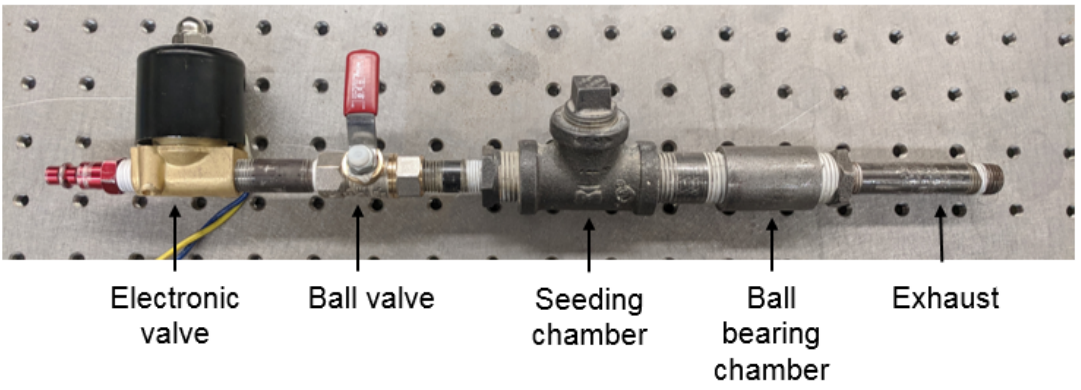

Figure 4.3: The solid particle diffuser pipe design for controlling particle dispersal.

A test setup was constructed to compare various solid particles for reflectivity. A large, clear acrylic box was placed over the diffuser to minimize particle scatter around the test area and quarantine aerosolized particulates as shown in Figure 4.4. Three solid particles were considered due to their availability and performance. These include: talcum powder, titanium dioxide, and hollow-glass spheres. Table 4.1 shows material data on these particle types. THOR's wall width of 10 cm was chosen as the characteristic length in the Stokes number calculation.

The particles were tested at various exposure durations for comparison. Talcum powder was initially chosen as the primary particle for dispersal due to its high reflectivity. In later explosive testing, hollow-glass spheres were used instead.

H

Table 4.1: Solid seeding particles specifications

Particle	Mean Diameter µm	Density (g/cc)	Refractive index	Stokes number
Talcum powder	14.3	2.7	1.6	0.164
Titanium dioxide	3 to 5	4.2	2.6	0.031
Hollow-glass spheres	8 to 12	1.05 to 1.15	0.21+2.62i	0.05

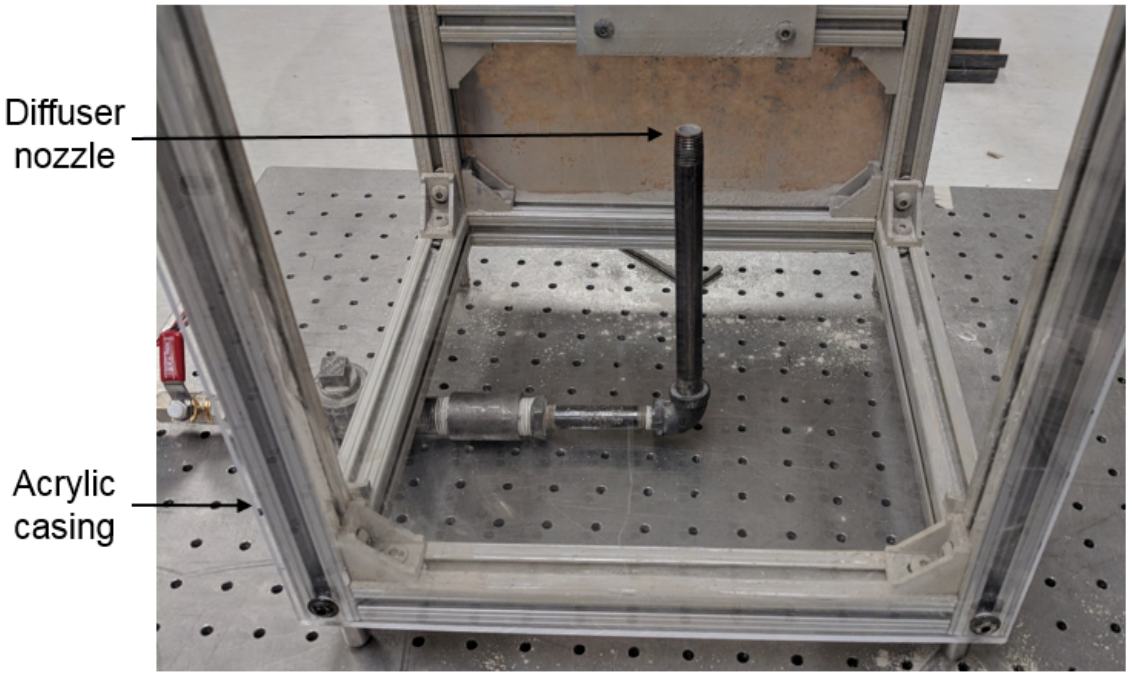

Figure 4.4: The particle diffuser placed inside a clear box.

4.2 Small-Scale Primer Testing

Initial testing began with shotgun primers as an explosive driver. The tests were conducted at 10,000 frames per second (fps) with 100 microsecond exposures. A Photron SA-X2 high-speed camera was used to record all test images.

Several particle dispersal methods were considered to determine ideal particle spread in the test section. The scenarios examined include: accumulations of particles placed in direct contact with the primer, particles dispersed inside shock tube prior to detonation, and particles dispersed prior to and during the detonation event. Of the dispersal techniques considered, particle dispersal prior to detonation was the most effective. Particles placed in direct contact with the detonator caused variable particle density in the test section. Applying particle

seeding in post-detonation caused flow disruptions and resulted in inaccurate velocity measurements.

An instantaneous velocity magnitude field was calculated with Insight 4G software using an interrogation window of 32 x 32 pixels. Figure 4.5 shows this velocity field alongside it's corresponding raw image. The images show talcum powder dispersed in air being driven by a shotgun primer detonation. The velocity vectors in the flow field indicate an incoming turbulent flow from the left, as expected. The instantaneous velocity field was calculated over a time interval of 100 microseconds.

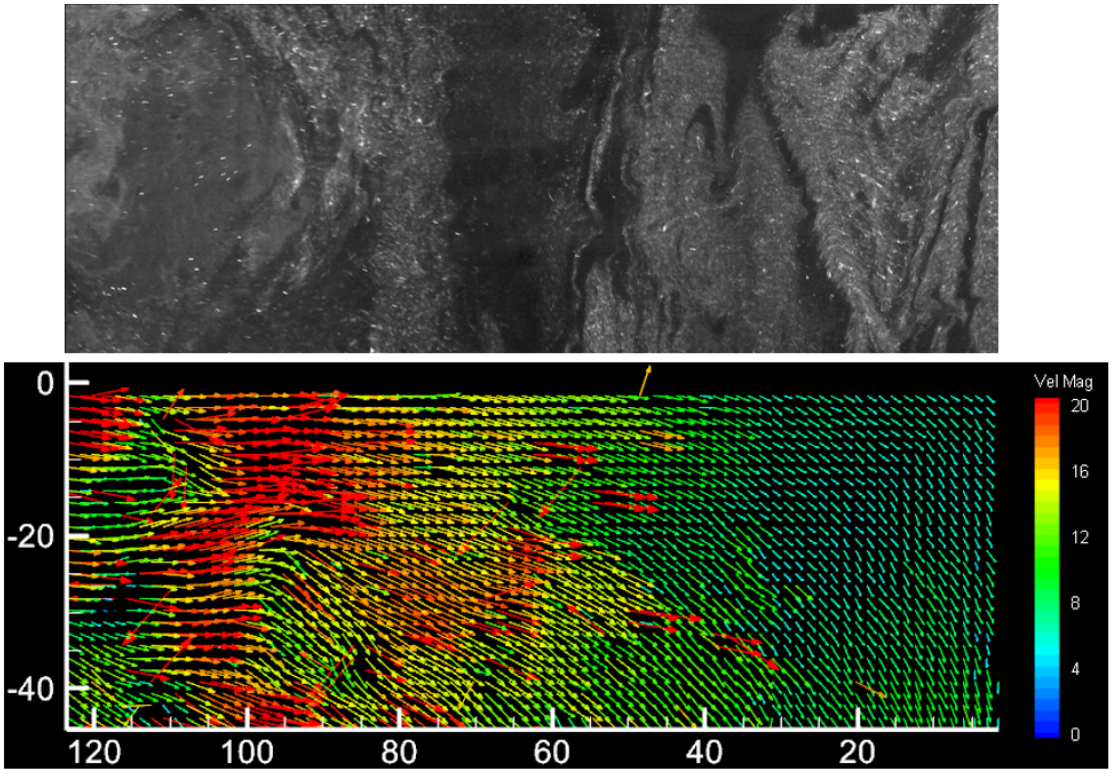

Figure 4.5: Raw image and instantaneous velocity flow field of talcum powder in air. Image scaling is in millimeters.

4.3 Identification of Shock Effects on Particles

Shock waves propagating through the suspended particles caused a breakup of individual particles. This resulted a fine particle cloud remaining in suspension after the shock wave had passed. The lack of singular, identifiable particle points did not allow proper tracking. This particle break-up effect was avoided

by changing the particle choice to hollow-glass spheres where the effect was minimized, because the agglomerations were better removed before the particles were suspended in the flow.

The light intensity of the MdL creates an upper-bound on the types of flows that can be captured. Exposure duration is the critical constraint that limits PIV in high-speed flows. With exposure durations of 10-20 microseconds, the passing shock wave causes a blurring of the particles as shown in Figure 4.6. This streaking makes PIV tracking of shock waves impractical with this exposure duration. The blurring effect can, however, still be used to locate the shock front. Manual hand calculation or edge detection can be used to approximate shock velocity from these images as demonstrated in Figure 4.6. The small-scale tests identified minimum exposure durations with the MdL to be around 10 microseconds. This exposure setting limits applications to high-speed flows.

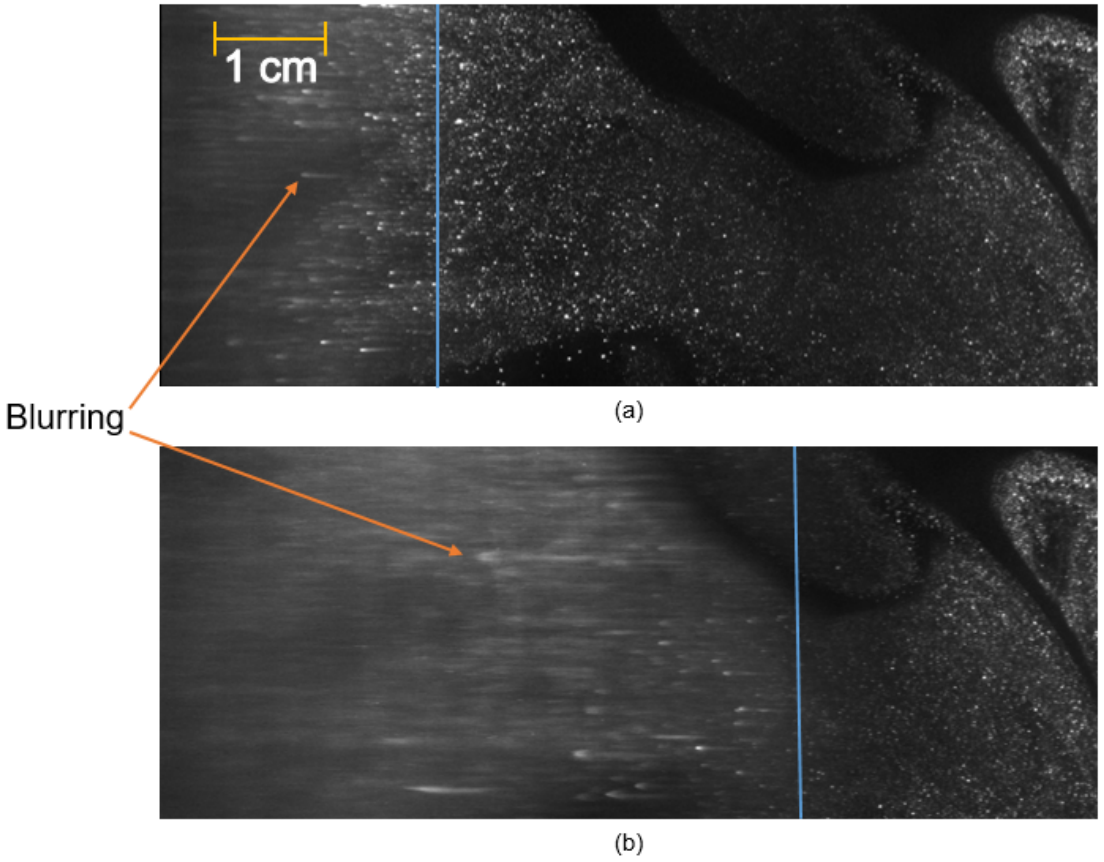

Figure 4.6: Blurring of particles caused by shockwave over Δt of 75 µ sec. The blue line indicates the approximate shock front location.

4.4 Explosive Turbulence Tracking in Shock Tube

The objective of this experiment series was to observe the turbulent gas motion in a post-blast detonation environment and perform PIV calculations on the recorded images. A RP-2 exploding bridgewire detonator with 50 mg of HE was used to drive a seeded flow in THOR. The detonator was inserted into a loading block and fixed into the driver section of THOR. Figures 4.7 and 4.8 show the composition of the detonator and its placement inside the loading block.

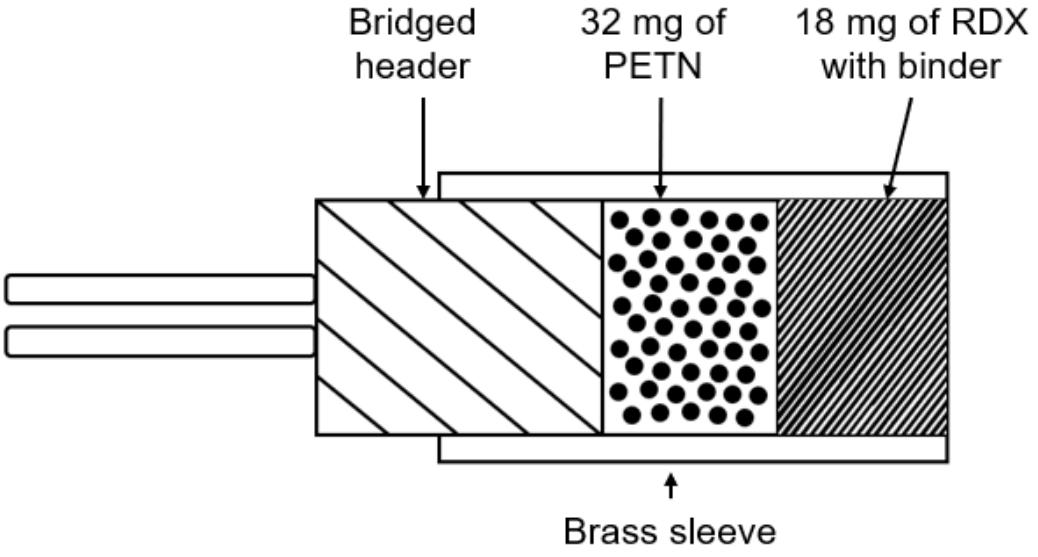

Figure 4.7: Diagram and composition of an RP-2 detonator.

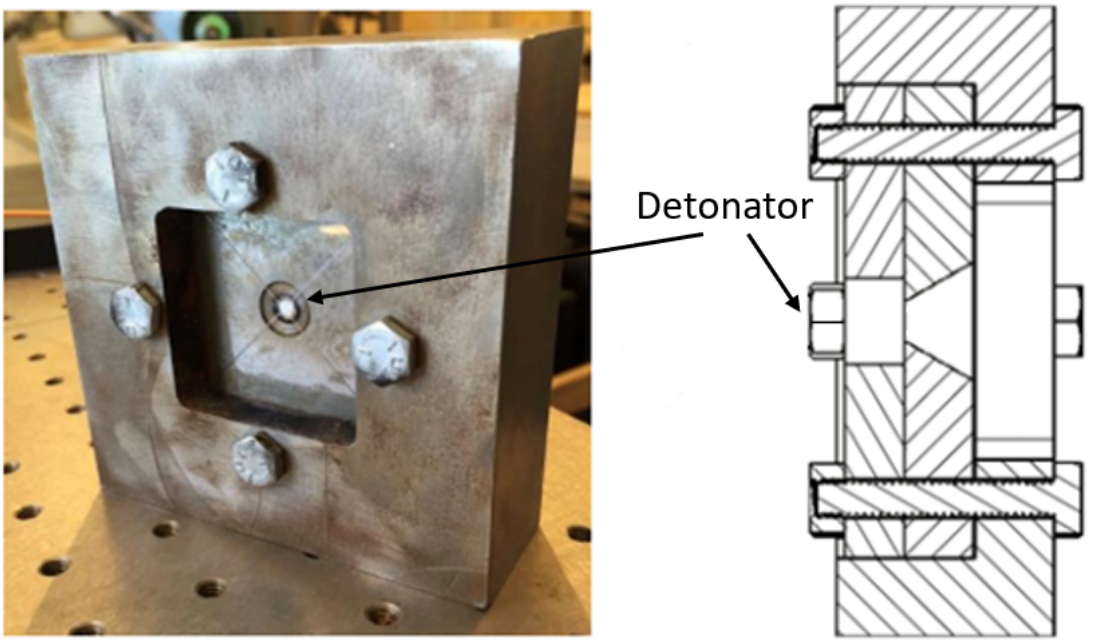

Figure 4.8: Placement of detonator inside the mounting block for THOR.

Images were captured at 40,000 fps with 10 or 20 microsecond exposures. An interrogation window of 24 x 24 pixels was used to process the turbulent flow. An average image intensity subtraction was performed to create higher contrast between the particles and the background. A post-processing routine removed erroneous vectors that were three standard deviations from the local mean.

Instantaneous measurements were performed at various times after detonation with a time interval of 25 microseconds between frames. Figure 4.9 shows the raw images captured with the SA-X2 camera. Figure 4.10 shows the corresponding instantaneous velocity magnitude vectors. Figure 4.11 shows the vorticity measurements at those time steps. The velocity vectors indicate an incoming flow from the left and show a velocity gradient in the range x = 50 - 70 mm. The corresponding vorticity field provide similar results showing high regions of vorticity in the same x = 50 - 70 mm range.

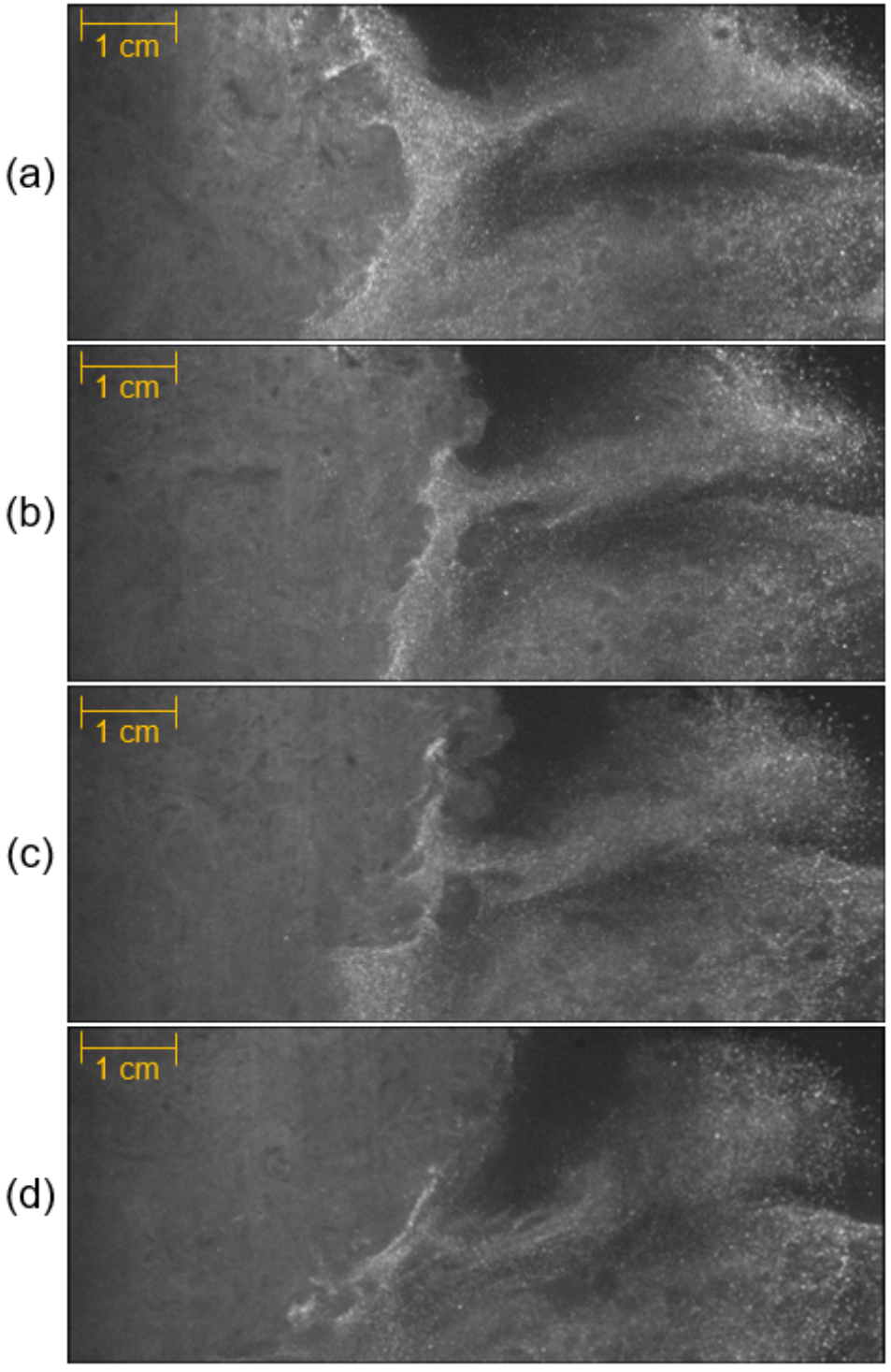

Figure 4.9: Histogram-stretched raw images at times (a) 8.75 ms (b) 9.75 ms (c) 10.75 ms (d) 11.75 ms after detonation

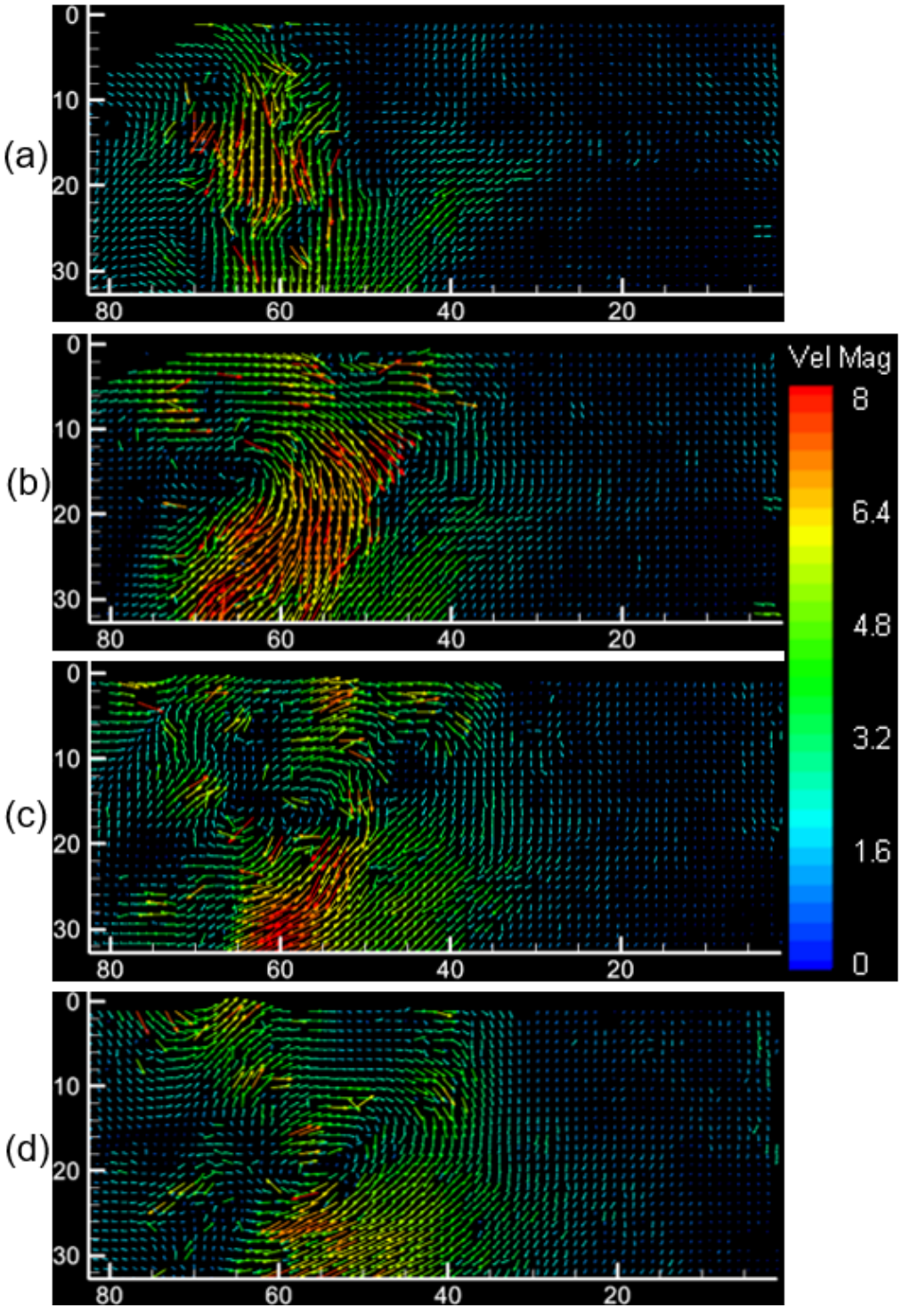

Figure 4.10: Instantaneous velocity magnitude vectors at times (a) 8.75 ms (b) 9.75 ms (c) 10.75 ms (d) 11.75 ms after detonation. Image scaling is in millimeters.

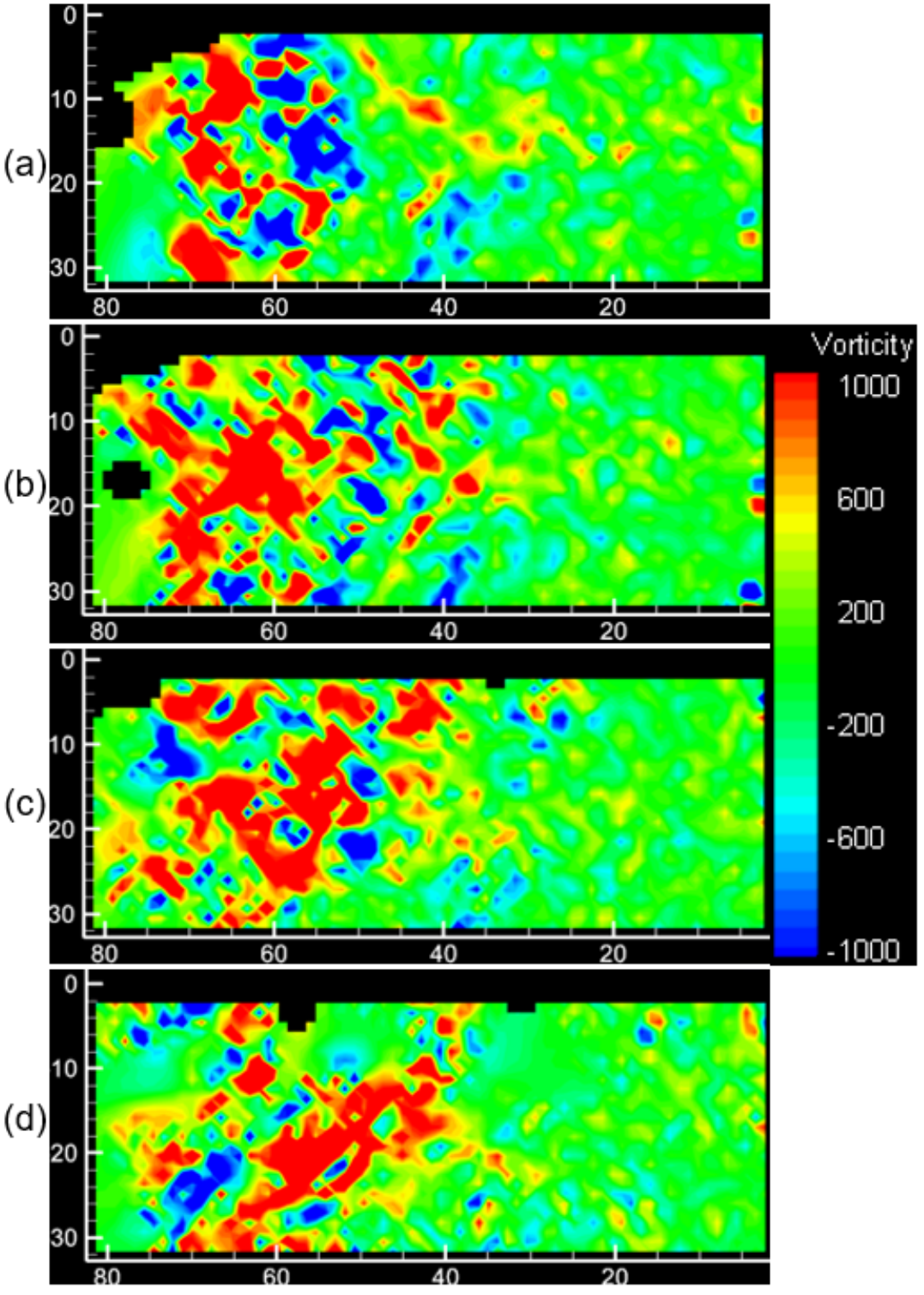

Figure 4.11: Vorticity measurements at times (a) 8.75 ms (b) 9.75 ms (c) 10.75 ms (d) 11.75 ms after detonation. Image scaling is in millimeters.

Time series analysis was performed on a single point in the observed region of interest over the duration of the explosive event. This analysis technique provides a visualization of changes in flow velocity or vorticity in a specific region during the post-blast environment. Figure 4.12 shows an example of time series analysis on a point. Vorticity was measured throughout the duration of the blast event for the indicated point location. The time analysis of the vorticity information provides a visualization of the arrival and dissipation of a vortex at that location. Time analysis techniques could be implemented to extract additional meaningful information to potentially gain characteristic insights into fluid flow behavior. These types of measurements demonstrate the capability of the MdL to provide time-resolved data of turbulence generated by high-speed flows.

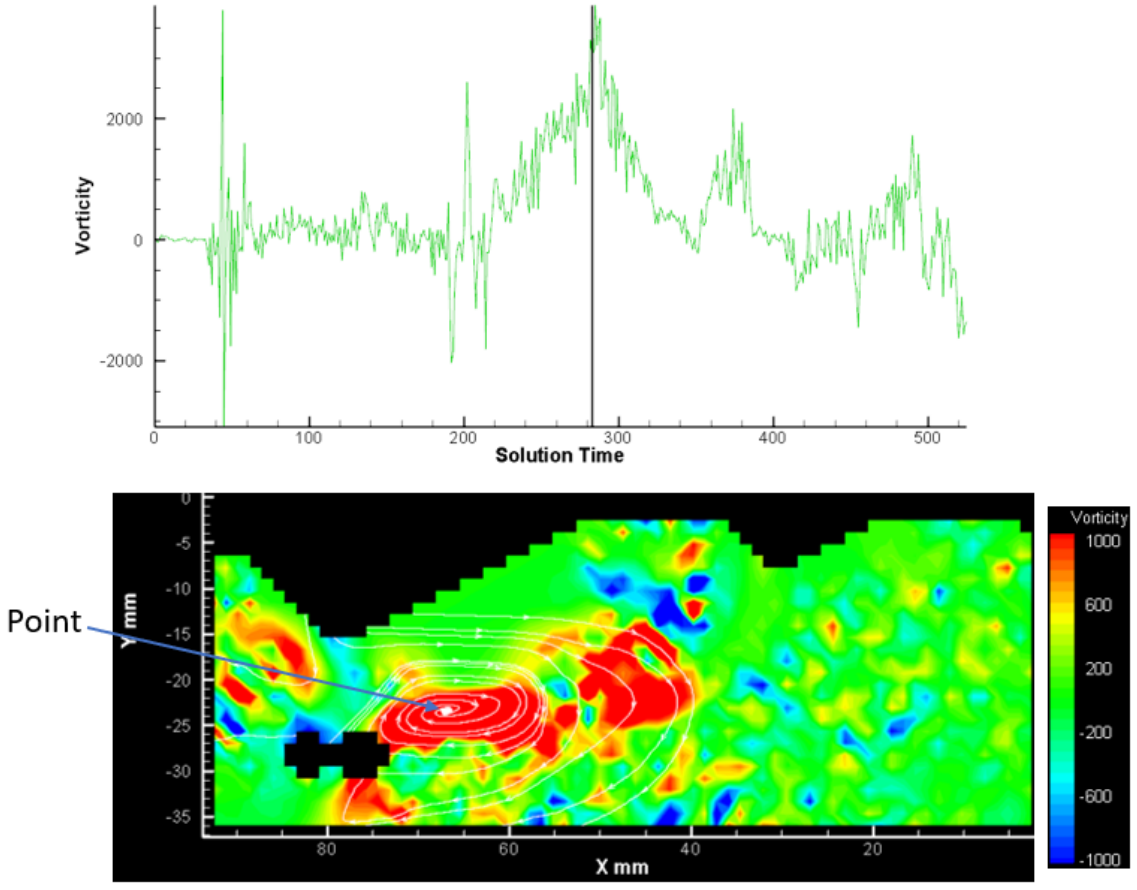

Figure 4.12: Time series analysis at a single point in post-blast environment. Black line denotes the time at which the corresponding vorticity map occurs.

CHAPTER 5

CONCLUSIONS AND FUTURE RESEARCH RECOMMENDATIONS

5.1 Conclusions

A low-cost device was constructed for performing steady and unsteady time-resolved imaging and particle image velocimetry (PIV). The device was constructed using 11 overlapping continuous lasers to generate a singular 2D light sheet for PIV applications. Glass rods were used as cylindrical lenses to transform the incoming laser beam into a 2D expanding light sheet. Individual lasers were placed into 6-DOF mounts to allow for accurate alignment in overlapping planes. The MdL housing was designed to allow horizontal and vertical mounting options.

The MdL was compared to an Nd:YAG laser to compare system accuracy. Steady flow testing in a water droplet seeded air flow demonstrated good agreement between the MdL and Nd:YAG laser, provided sufficient particle density and illumination intensity are achieved. A T-test analysis between velocity profiles from both lasers yielded similar conclusions. Error analysis indicated an increasing bias error at larger x/D distances from the nozzle. Analogous RMS errors were produced from both laser systems in the centerline regions of the flow. The similar RMS errors throughout the velocity profiles indicate that bias error is a function of varying test conditions or MdL alignment and not caused by deficiencies in light intensity.

Unsteady testing was performed with RP-2 detonators to observe and measure turbulence in a post-blast environment. Hollow-glass spheres were used to seed the unsteady flow region due to their high reflectivity. Results indicate good accuracy in particle tracking in lower velocity regions of the flow. Unsteady testing revealed limitations in the MdL design including an exposure duration of 10 microseconds, making particle tracking in supersonic flows impractical.

5.2 Future Research

The MdL offers a significant advantage over traditional PIV lasers by providing time-resolved data. The MdL can provide a better understanding of fluid

motion by incorporating seeded (PIV) and non-seeded (SIV) measurement techniques in flow visualization and measurement.

The small acrylic housing allowed for easy mounting but made laser adjustment difficult. A larger housing design would allow for easier laser position alignment. The low-cost lasers implement low quality optics and components, which should be upgraded to ensure reliability. Additionally, the low power output of these lasers limited particle selection and viewable flow velocities. Installing fewer higher-powered lasers would allow for easier alignment and operation and could allow for imaging at lower exposure durations. However, overheating from increased power consumption can cause deformation in the acrylic components of the MdL.

To visualize natural turbulent phenomena in a detonation environment, open-air field testing needs to be conducted. The portable design of the laser allows for easy transport and setup but, the low power output and small region of interest will limit outdoor applications. Additional obstacles include: fine DOF alignment in an outdoor setting, strong vibrations causing misalignment in laser or lens position, and vibrations causing structural damages to the acrylic housing.

REFERENCES

[1] Alexander J Smits. *Flow visualization: techniques and examples*. World Scientific, 2012.

[2] James Scott Anderson. Study of turbulent mixing in a post detonation environment using schlieren and imaging spectroscopy. Master's thesis, New Mexico Institute of Mining and Technology, 2017.

[3] Stefano Discetti, Andrea Ianiro, Tommaso Astarita, and Gennaro Cardone. On a novel low cost high accuracy experimental setup for tomographic particle image velocimetry. *Measurement Science and Technology*, 24(7):075302, 2013.

[4] Novica Z Janković, Marko C Barjaktarović, Milica M Janković, and Djordje S Čantrak. First steps in new affordable piv measurements. In *Telecommunications Forum (TELFOR), 2016 24th*, pages 1–4. IEEE, 2016.

[5] William G Ryerson and Kurt Schwenk. A simple, inexpensive system for digital particle image velocimetry (dpiv) in biomechanics. *Journal of Experimental Zoology Part A: Ecological Genetics and Physiology*, 317(2):127–140, 2012.

[6] Mr Brock Philip Ring and Evan C Lemley. Design and implementation of a low cost particle image velocimetry system for undergraduate research and education. *age*, 24:1, 2014.

[7] T Dwayne McCay and JA Roux. *Combustion diagnostics by nonintrusive methods*, volume 92. Amer Inst of Aeronautics &, 1984.

[8] Wolgang Merzkirch. *Flow visualization*. Elsevier, 2012.

[9] Markus Raffel, Christian E Willert, Fulvio Scarano, Christian J Kähler, Steve T Wereley, and Jürgen Kompenhans. *Particle image velocimetry: a practical guide*. Springer, 2018.

[10] Cameron Tropea and Alexander L Yarin. *Springer handbook of experimental fluid mechanics*, volume 1. Springer Science & Business Media, 2007.

[11] Martin J Rhodes and Martin Rhodes. *Introduction to particle technology*. John Wiley & Sons, 2008.

[12] Ludwig Prandtl. Über flussigkeitsbewegung bei sehr kleiner reibung. *Verhandl. III, Internat. Math.-Kong., Heidelberg, Teubner, Leipzig, 1904*, pages 484–491, 1904.

[13] Christian E Willert and Morteza Gharib. Digital particle image velocimetry. *Experiments in fluids*, 10(4):181–193, 1991.

[14] N Hamel, A de Champlain, P-A Rainville, D Kretschmer, P Gaudreau, S Bouziane, R Farinaccio, and R Stowe. Supersonic piv measurements in an open jet flow. In *37th Joint Propulsion Conference and Exhibit*, page 3527, 2001.

[15] Fulvio Scarano. Overview of piv in supersonic flows. In *Particle Image Velocimetry*, pages 445–463. Springer, 2007.

[16] Charles M Jenkins, Yasuyuki Horie, and Chang-Yu Wu. Particle velocity and structures in blast waves imaged using particle image velocimetry. *International Journal of Multiphase Flow*, 1(36):88–91, 2010.

[17] Charles M Jenkins, Robert C Ripley, Chang-Yu Wu, Yasuyuki Horie, Kevin Powers, and William H Wilson. Explosively driven particle fields imaged using a high speed framing camera and particle image velocimetry. *International Journal of Multiphase Flow*, 51:73–86, 2013.

[18] Michael J Murphy and Ronald J Adrian. Piv space-time resolution of flow behind blast waves. *Experiments in Fluids*, 49(1):193–202, 2010.

[19] Piv systems. http://tsi.com/piv-systems/. Accessed: 2018-07-17.

[20] Mohsen Jahanmiri. Particle image velocimetry: Fundamentals and its applications. Technical report, Chalmers University of Technology, 2011.

[21] Ajay K Prasad. Particle image velocimetry. *CURRENT SCIENCE-BANGALORE-*, 79(1):51–60, 2000.

[22] Laser quantum. https://www.laserquantum.com/products/#. Accessed: 2018-07-21.

[23] Ronald J Adrian. Twenty years of particle image velocimetry. *Experiments in fluids*, 39(2):159–169, 2005.

[24] GS Settles. Schlieren and shadowgraph techniques: visualizing phenomena in transparent media, 2002.

[25] Michael J Hargather and Gary S Settles. Retroreflective shadowgraph technique for large-scale flow visualization. *Applied optics*, 48(22):4449–4457, 2009.

[26] PM Giannuzzi, MJ Hargather, and GC Doig. Explosive-driven shock wave and vortex ring interaction with a propane flame. *Shock Waves*, 26(6):851–857, 2016.

[27] Kyle Winter. Three-dimensional shock wave reconstruction using multiple high-speed digital cameras and background oriented schlieren imaging. Master's thesis, New Mexico Institute of Mining and Technology, 2018.

[28] H C H Townend. A method of air flow cinematography capable of quantitative analysis. *Journal of the Aeronautical Sciences*, 3(10):343–352, 1936.

[29] Dennis R Jonassen, Gary S Settles, and Michael D Tronosky. Schlieren âĂIJpivâĂİ for turbulent flows. *Optics and Lasers in Engineering*, 44(3-4):190–207, 2006.

[30] Michael J Hargather, Michael J Lawson, Gary S Settles, and Leonard M Weinstein. Seedless velocimetry measurements by schlieren image velocimetry. *AIAA journal*, 49(3):611–620, 2011.

[31] Rudy Morales. Schlieren image velocimetry measurements in a rocket engine exhaust plume. Master's thesis, New Mexico Institute of Mining and Technology, 2018.

[32] Joshua L Smith. Design and construction of a fixture to examine the explosive effects of al/i 2 o 5. Master's thesis, New Mexico Institute of Mining and Technology, 2016.

[33] Insight 4g global image, acquisition, analysis, and display software. http://www.tsi.com/. Accessed: 2018-07-17.

[34] Thomas L Labus and Eugene P Symons. Experimental investigation of an axisymmetric free jet with an initially uniform velocity profile. 1972.

[35] Hendrik Tennekes, John Leask Lumley, JL Lumley, et al. *A first course in turbulence*. MIT press, 1972.

DEVELOPMENT OF A LOW-COST, MULTIPLE-DIODE, CONTINUOUS LASER FOR PIV APPLICATIONS

by

Rajkumar Bhakta